Anode partial flooding modelling of proton exchange membrane fuel cells: Model development and validation

Anode partial flooding modelling of Proton Exchange Membrane Fuel Cells: Model development and validation

Lei Xing[a,b,*], Shangfeng Du[b], Rui Chen[c], Mohamed Mamlouk[d] and Keith Scott[d]

a. School of Chemical Engineering, University of Birmingham, Edgbaston, Birmingham, B15 2TT, United Kingdom

b. School of Chemical Engineering, Inner Mongolia University of Technology, Hohhot, 010051, China

c. School of Aeronautical and Automotive Engineering, Loughborough University, Leicestershire, LE11 3TU, United Kingdom

d. School of Chemical Engineering and Advanced Materials, Merz Court, Newcastle University, Newcastle upon Tyne, NE1 7RU, United Kingdom

Highlights

- A fully coupled 2D, along-the-channel, two-phase flow, non-isothermal, CFD model is developed.

- Temperature rise due to electrochemical reactions, ohmic resistance and water phase-transfer is analysed.

- Mathematical expressions of liquid water saturation against current density at anode and cathode are regressed.

- Relationship between the liquid water saturation at anode and cathode is built.

Corresponding author:

School of Chemical Engineering, University of Birmingham, Edgbaston, Birmingham, B15 2TT, United Kingdom
Tel.: +44 (0)121 414 5081
Fax: +44 (0)121 414 5081
Email: xinglei1314@gmail.com; l.xing@bham.ac.uk

Shangfeng Du (S.Du@bham.ac.uk)
Rui Chen (r.chen@lboro.ac.uk)
Mohamed Mamlouk (m.mamlouk@ncl.ac.uk)
Keith Scott (k.scott@ncl.ac.uk)

Abstract

A two-dimensional along-the-channel computational fluid dynamic (CFD) model, coupled with a two-phase flow model of liquid water and gas transport for a proton exchange membrane (PEM) fuel cell is described. The model considers non-isothermal operation and thus the non-uniform temperature distribution in the cell structure. Water phase-transfer between the vapour, liquid water and dissolved phase is modelled with the combinational transport mechanism through the membrane. Liquid water saturation is simulated inside the electrodes and channels at both the anode and cathode sides. Three types of models are compared for the hydrogen oxidation reaction (HOR) and oxygen reduction reaction (ORR) in catalyst layers, including Butler-Volmer (B-V), liquid water saturation corrected B-V and agglomerate mechanisms. Temperature changes in membrane electrode assembly (MEA) and channels due to electrochemical reaction, ohmic resistance and water phase-transfer are analysed as a function of current density. Nonlinear relations of liquid water saturations with respect to current densities at both the anode and cathode are regressed. At low and high current densities, liquid water saturation in the anode linearly increases as a consequence of the linear increase of liquid water saturation in the cathode. In contrast, exponential relation is found to be more accurate at medium current densities.

Key works: PEMFC; liquid water; anode flooding; agglomerate model; non-isothermal; CFD

1. Introduction

Benefiting from high energy efficiency and low emission, proton exchange membrane fuel cells (PEMFCs), play an important role in transiting a carbon intensive economy to sustainable low carbon future [1-4]. In addition, the features of PEMFCs endow a flexibility and scalability for use with batteries and combined heat and power (CHP) system for hybrid automotive and residential use [5-7], as well as energy conversion between winds to electricity [8]. Among the PEMFC family, the medium and low temperature PEMFCs are considered as promising candidates as portable and automotive power sources. However, they can experience certain operating difficulties associated with water transport and flooding during their operation, especially at a high current density [9-11].

Three phases of water co-exist in PEMFCs: as vapor and liquid in porous electrodes and channels, and as a dissolved phase absorbed by membrane and ionomer (membrane and ionomer water uptake). Among three phases, dissolved water can migrate between both electrodes through the membrane under the driving forces of electro-osmotic drag (EOD), back diffusion and hydraulic permeation [12-14]. Liquid water can be generated in terms of water vapor condensation and membrane/ionomer desorption when over-saturated. Simultaneously, liquid water is removed from the MEA (membrane electrode assembly) generally by reactant gases flowing along the channels. If water generation rate is faster than the removal rate, excess water will accumulate in the electrodes and flow channels, leading to a water flooding inside the cell. This flooding can reduce the effective porosity in the porous media and increase the pressure drop along the channel, inhibiting the gas transport to the active sites in catalyst layers (CLs), finally resulting in a decline in the cell performance [15-17]. Water flooding is typically observed at the cathode side due to the fact that water is produced inside the cathode catalyst layers (CCLs) by the oxygen reduction reaction (ORR).

There have been numerous studies of water flooding at the cathode but less consideration of water transport related to the anode. However, hydrogen consumption at the anode could also results in the humidified anode reactant gas becoming supersaturated with water vapor, which can result in transfer to liquid water after condensation. Liquid water movement in hydrophilic and hydrophobic anode gas channel, as well as the effect of hydrogen inlet velocity, operating temperature and channel walls wettability, was numerically studied by Ferreira et al. [18]. Experimental studies have detected liquid water in the anode and that more liquid water was observed at a high anode relative humidity [19, 20]. An in-situ detection scheme of anode flooding, developed by O'Rourke et al. [21], showed that anode flooding could be detected prior to a rapid cell voltage decline, which was considered as an early warning of cathode catalyst damage. As reported by Anderson et al. [22], anode water removal (AWR) could be used as a diagnostic tool to assess cathode water flooding in PEM fuel cells.

Catalyst layers are complex structures and are a difficult to describe and be fully understood in PEMFCs; not only due to their highly compact structure and complex composition but also because of the coupled electrochemical reactions and transport processes occurred. CLs in PEMFCs facilitate electrochemical reactions and produce water at the cathode. To describe the current density produced on each electrode in fuel cell operation, considering the water generated which can partially cover the platinum catalyst surface, (1-s) corrected B-V equation (s is the liquid water saturation, defining as the volume fraction of void space occupied by liquid water) is usually required instead of the traditional B-V equation [23-25]. The electrochemical activity may be further represented using an agglomerate mode, taking into account the increase in ionomer film thickness surrounding the agglomerate due to ionomer swelling. Furthermore, by considering gas transport resistance and the reduction of porosity

102   due to liquid water occupation, the agglomerate model can also provide a superior representation of

103   the porous CLs in comparison with other models [26, 27].

104   In fuel cell operation, temperature plays a significant role in achieving a high power performance. A

105   variety of parameters, e.g. electrochemical reaction kinetics, mole fractions in gas mixture, electrolyte

106   conductivity, rate of mass transfer, as well as liquid water saturation, are closely correlated with

107   temperature during fuel cell operation. Within PEMFCs, the temperature distribution across the MEAs

108   and along the flow channels can be either estimated by mathematical modelling technique or detected

109   by experimental measurements [28-31]. Ju et al. [28] developed a three dimensional (3D),

110   single-phase, non-isothermal model through a parametric study for GDL thermal conductivity, gas

111   relative humidity and operating cell voltage. Wang et al. [29] measured the temperature profile within

112   a single PEMFC with the aid of infrared thermal imaging (ITI) and found that the downstream

113   temperature is higher than the upstream, and there was an obvious high temperature section in the

114   outlet of oxygen. Temperature measurement were conducted by Zhang et al. [30] and Lin et al. [31]

115   from which they found a correlation between local temperature rise and local current density, and a

116   temperature rise at backsides of both the anode and cathode flow field plates.

117   However, up to now, it is still a challenge to fully couple most aspects mentioned above in

118   modelling for a highly accurate evaluation of water flooding in a single PEMFC or stack. In this paper,

119   we fully couple seven sub-models and apply them on a two dimensional (2D), along-the-channel

120   (ATC) geometry for a single PEMFC: (1) agglomerate models for gas transport resistance in CLs, (2)

121   two-phase flow models for liquid water saturation, (3) combinational diffusion models for dissolved

122   water transport through the membrane, (4) non-isothermal models for heat transport in MEA and

123   channels, (5) computational fluid dynamic (CFD) models for gas transport along the channels, (6)

124   multicomponent diffusion of reactant gases in gas mixture, and (7) ionomer swelling due to

125   non-uniform distribution of water content. The effect of liquid water on the current density are

126   compared based on three mechanisms, including traditional B-V, (1-s) corrected B-V and agglomerate

127   kinetics. Distributions of reactant gas, liquid water and heat within the cell are investigated. The

128   expressions for the relationship between the liquid water saturation on each electrode and current

129   density, as well as the liquid water saturation between anode and cathode, are regressed.

2. Model description

2.1 Assumption

132   Some additional assumptions were employed in this work in addition to those in the previous

133   papers [35-39]:

134   1. Steady state, two-phase flow, along the channel model of a PEMFC.

135   2. Gas flow in the channels is laminar flow and incompressible.

136   3. Reactant gases enter the gas channels in a direction normal to the channel cross section.

137   4. Liquid water saturation in channels is continuous.

138   5. Gas diffusion layers and catalyst layers are isotropic.

139   6. No liquid water enters the channels at the inlets.

140   7. Same electrodes and bipolar plates are used in the anode and cathode, respectively.

2.2 Governing equations

142   The conservation equations of mass, momentum, species, energy and charges are summarized as Eqns.

143   (1) to (4):

144    $$\nabla \cdot (\rho^g \mathbf{u}^g) = S_m \tag{1}$$

145 $$\rho^g (\mathbf{u}^g \cdot \nabla \mathbf{u}^g) = \nabla \left[-pI + \mu^g \nabla \mathbf{u}^g + \mu^g (\nabla \mathbf{u}^g)^T - \frac{2}{3} \mu^g (\nabla \cdot \mathbf{u}^g)I \right] \qquad (2)$$

146 $$\rho^g \mathbf{u}^g \cdot \nabla w_i^g - \nabla \cdot [\rho^g \sum_{j=1}^{N} (1-s^{'}) D_{ij} (\nabla x_j^g - w_j^g) \frac{\nabla p}{p} + D_i^T \frac{\nabla T}{T}] = M_i S_i^g \qquad (3)$$

147 $$\nabla \cdot [\sum_{i=g,l} (\varepsilon \rho c_p \mathbf{u})_i T] - \nabla \cdot (\sum_{i=g,l,s} k_i \nabla T) = S_T \qquad (4)$$

148 $$\sigma_s^{eff} \nabla \cdot \nabla \varphi_s + \sigma_M^{eff} \nabla \cdot \nabla \varphi_M = 0 \qquad (5)$$

149 where ρ (kg m^{-3}) is density, $\mathbf{u}$ (m s^{-1}) is velocity, p (Pa) is pressure, μ (Pa s) is viscosity, M

150 (kg mol^{-1}) is molecular weight, D (m^2 s^{-1}) is diffusion coefficient, D^T (kg m^{-1} s^{-1}) is thermal

151 diffusion coefficient, c_p (J mol^{-1} K^{-1}) is specific heat capacity, k (W m^{-1} K^{-1}) is thermal

152 conductivity, T (K) is temperature, σ (S m^{-1}) is conductivity φ (V) is potential. w is mass

153 fraction, x is mole fraction, ε is volume fraction, $s^{'}$ is corrected liquid water saturation and I

154 is identity matrix. Subscript i and j represent species i and j and superscript g means gas phase. S is

155 the source term, which is given in detail in Tables 1 to 3. Note that Eq. (1) to Eq. (3) were applied on

156 reactant gas only and the gas velocity in porous electrodes could be related to pressure according to

157 Darcy's law as below:

158 $$\mathbf{u}^g = -\frac{k_p}{\mu^g} \nabla p \qquad (6)$$

159 where k_p (m^2) is the permeability of the porous media.

160 For the purpose of describing dissolved and liquid water transport, the following equations were used.

161 $$\nabla \cdot (n_d \frac{i_M}{F}) - \nabla \cdot (D_{w-M} \nabla c_w^d) - \nabla \cdot (\frac{k_{p,M} c_w^d}{\mu_w} \nabla p) = S_w^d \qquad (7)$$

162 $$\nabla \cdot (\rho_w^l D_c \nabla s - \frac{\rho_w^l k_r^l \mu_w^g}{k_r^g \mu_w^l} \mathbf{u}^g) = M_w S_w^l \qquad (8)$$

163 Eq. (7) was developed by applying the diffusive approach to a conservation equation of dissolved

164 water, while Eq. (8) was obtained by applying the volume average approach to the continuity equation

165   and using Darcy's law for both the liquid and gas phases.

166   The capillary diffusion coefficient, D_c (m^2 s^{-1}), was calculated using Eq. (9) [32]:

167
$$D_c = -\frac{k_r^l}{\mu_w^l} \sigma \cos(\theta_c)(\varepsilon k_p)^{1/2} \frac{dJ(s)}{ds} \qquad (9)$$

168   where k_r^l is the relative permeability of liquid phase, μ_w^l (Pa s) is the dynamic viscosity of liquid

169   water, σ (N m^{-1}) is the surface tension, θ_c (°) is the contact angel, ε is the porosity of the electrode,

170   k_p (m^2) is the permeability of the porous electrode, $J(s)$ is the Leverett function.

171   The equilibrium membrane/ionomer water content, determined based on water uptake measurement,

172   is given as [33]:

173    $$\lambda^{eq} = 16.8s + 14.0(1-s) \qquad s > 0 \qquad (10)$$

174   The permeability of gas channels was calculated by Hagen-Poiseuille equation [34].

175
$$k_{p,ch} = \frac{c_{sf} d_h^2}{32} \qquad (11)$$

176   where c_{sf} is the flow shape factor (1.127 for a square cross-section) and d_h is the hydraulic

177   diameter of a channel, which can be calculated by the relation of the cross-sectional area and wetted

178   perimeter.

179   The electrochemical reactions inside the catalyst layers according to three different mechanisms,

180   including B-V, (1-s) corrected B-V and agglomerate assumption, can be written as below:

181
$$i_{BV} = a_{agg}^M i_{0,i}^{ref} (\frac{p_i}{c_i^{ref} H_i})^\gamma \left[\exp(\frac{-\alpha_{Rd,i} F \eta_i}{RT}) - \exp(\frac{\alpha_{Ox,i} F \eta_i}{RT}) \right] \qquad (12)$$

182
$$i_{(1-s)BV} = (1-s) a_{agg}^M i_{0,i}^{ref} (\frac{p_i}{c_i^{ref} H_i})^\gamma \left[\exp(\frac{-\alpha_{Rd,i} F \eta_i}{RT}) - \exp(\frac{\alpha_{Ox,i} F \eta_i}{RT}) \right] \qquad (13)$$

183
$$i_{agg} = nF(\frac{p_i}{c_i^{ref} H_i})^\gamma \left[\frac{1}{E_{agg} k_{agg}} + \frac{(r_{agg} + \delta_M + \delta_w)}{r_{agg}} (\frac{\delta_M}{a_{agg}^M D_{O_2-M}} + \frac{\delta_w}{a_{agg}^w D_{O_2-w}}) \right]^{-1} \qquad (14)$$

184   where

185 $$k_{agg} = \frac{a_{agg}^M i_{0,i}^{ref}}{nF} \left[\exp(\frac{-\alpha_{Rd,i} F \eta_i}{RT}) - \exp(\frac{\alpha_{Ox,i} F \eta_i}{RT}) \right]$$ (15)

186 The subscript i is for anode and cathode, respectively, and the superscript γ equals to 0.5 for hydrogen

187 oxidation reaction (HOR) in anode and 1.0 for ORR in cathode. The properties of the catalyst layer

188 (porosity, specific area, ionomer and water film thickness), gas transport through the porous electrode

189 (species diffusion in gas mixture and Knudsen diffusion), numerous key parameters and fundamental

190 equations, were listed in Table 4. Details can be found in literature [35-39].

2.3 Boundary conditions

192 At anode inlet (A'-B') and cathode inlet (G-H) as shown in Fig. 1, the temperature, mole fractions of

193 reactant gases in gas mixture, and liquid water saturation are given as below:

194 $$T = T^{cell}, \quad x_{w,a}^0 = \frac{p_{sat} RH_a}{p_a}, \quad x_{H_2}^0 = 1 - x_{H_2O,a,in}, \quad s_a = 0$$ (16)

195 $$T = T^{cell}, \quad x_{w,c}^0 = \frac{p_{sat} RH_c}{p_c}, \quad x_{O_2}^0 = 0.21(1 - x_{H_2O,c,in}), \quad x_{N_2}^0 = 0.79(1 - x_{H_2O,c,in}), \quad s_c = 0$$ (17)

196 The gas velocities at the inlets of both electrodes are related to their stoichiometry shown as follow:

197 $$\mathbf{u}_a^{g,0} = \frac{\xi_a RT i^{ref} A_M}{2F p_a x_{H_2} A_{ch}}, \quad \mathbf{u}_c^{g,0} = \frac{\xi_c RT i^{ref} A_M}{4F p_c x_{O_2} A_{ch}}$$ (18)

198 where i^{ref} is the reference current density (defined as 1.0 A cm^{-2} in this study), ξ_a and ξ_c are the

199 stoichiometry of the anode and cathode, respectively. A_M (m^2) and A_{ch} (m^2) are the effective area of

200 electrode and the cross-sectional area of channel, respectively.

201 At the inlet and outlet of both the anode and cathode, the pressure was given as a boundary condition.

202 $$p_a = p_a^0, \quad p_c = p_c^0$$ (19)

203 The water content on the CL-membrane interfaces of anode (C-C') and cathode (F-F') were defined

204 as Dirichlet boundaries with the values according to the following equations [14, 37-39]:

205 $$\lambda = 0.043 + 17.81\alpha_w - 39.85\alpha_w^2 + 36.0\alpha_w^3 \qquad (20)$$

206 $$\alpha_w = x_w \frac{p}{p_{sat}} + 2s \qquad (21)$$

2.4 Numerical solution

208   The numerical solution of the fully coupled governing equations was based on the finite element

209 method (FEM). First of all, mesh was developed over the computational domain by dividing it into

210 numerous elements. The distance between each element is known as the step. At each step, the

211 equations accounting for different phenomena were fully coupled and computed with the boundary

212 conditions. Initial value was given to each parameter at the first attempt then followed by an iterative

213 process until the calculation error was smaller than 10^{-5}. Commercial software COMSOL

214 Multiphysics 4.4 was used to implement the fully coupled equations. The key to successfully solving

215 this model is simulating the membrane/ionomer water content, which significantly affects many

216 critical parameters, i.e. ionomer volume fraction, EOD coefficient, ionic conductivity, hydraulic

217 permeability and water diffusivity.

2.5 Mesh independence

219   Theoretically, the computation error in the solution related to the grid must disappear for an

220 increasingly fine mesh. The effect of mesh on the final simulation results is more significant at high

221 current density due to the increasing impact of mass transport. The current density at a low cell

222 voltage (0.2 V) was therefore taken as the parameter to evaluate nine mesh grids (see Table 5) and

223 determine the influence of the element number on the solution. In this study, the number of elements

224 on various computational domains, including flow channel, GDL, CL and membrane, was

225 investigated with a fixed number of elements (250) along the channel [36]. Three levels of element

226 numbers were studied in each domain, which guaranteed the total number of element increasing at

227 1×10^4 each time. Fig. 2 shows that the current density reaches an asymptotic value while the

228 computation duration increases as the number of elements increases. The current density almost kept

229 as a constant when a finer mesh as Grid 7 was applied. A relative rapidly increase in computational

230 duration was observed from Grid 5 to Grid 7. This indicated that the time consuming step among the

231 computational process was in the catalyst layers, in which numbers of transport and electrochemical

232 processes were involved. In order to reduce the calculation error, finer mesh has to be developed on

233 catalyst layers. Having balancing both the computational accuracy and duration, Grid 6 was selected

234 considering a sufficient reliability to ensure mesh independence with acceptable calculating time.

235 # 3. Results and discussions

236 ## 3.1 Model validation

237 Fig. 3 shows the comparison of the simulation results with experimental data obtained both

238 in-house and selected from literature [41]. For the in-house case shown in Fig. 3(a), the anode and

239 cathode catalyst layers were made from 20% Pt/C with a Pt loading of 0.1 and 0.4 mg cm^{-2},

240 respectively. 5% Nafion® ionomer solution in de-ionized water was used as binder. The ionomer mass

241 ratios were 20% in the catalyst layers at both the anode and cathode. Nafion® 112 membrane was used

242 as electrolyte sandwiched between anode and cathode. The graphite plates with an active area of 1.0

243 cm × 1.0 cm were grooved with serpentine gas channels with a dimension of 0.1 cm × 0.1 cm. For the

244 case in Fig. 3(b), 40% Pt/C with a platinum loading of 0.4 mg cm^{-2} was used. Serpentine flow field

245 was applied as well with a dimension of the 0.1 cm × 0.1 cm and an active area of 7.2 cm × 7.2 cm.

246 For the formal case, the cell was tested with the cell and gas inlet temperatures at 80 °C under a

247 hydrogen flow rate of 200 sccm at the anode side and an air flow rate of 500 sccm at the cathode side.

248 For the latter case, cell and gas inlet temperatures were 70 °C with the hydrogen flow rate of 1200

249   sccm and air flow rate of 2200 sccm. Reactant gas pressure and humidity were kept at 1.0 atm and

250   100% for both cases. The parameters used for model validation and base case in this study are listed

251   in Table 6. The cathode transfer coefficient (α_c) was obtained by fitting the experimental polarisation

252   curves in the kinetics control zone (cell voltage higher than 0.8 V) and the obtained α_c was further

253   verified by the Tafel slope worked out in the model [40]. More details of the membrane electrode

254   assembly (MEA) preparation and cell test can be found elsewhere [37-39, 41].

255   A good agreement between the simulation results and the experimental data is indicated by Fig. 3 at

256   higher cell voltages, corresponding to lower current densities, due to the slow reaction rate and

257   insignificant mass transport impact. There was a typical drop in cell voltage due to various losses in

258   terms of activation polarization loss, ohmic loss and concentration polarization loss, as the current

259   density increased. A more rapid drop in current density, caused by the increasing mass transport

260   resistance, was observed at high current densities (mass transport control zone), where the departures

261   of simulation results compared with experimental data was clearly observed. The rapid decrease in

262   current density can be explained by the increase in mass transfer losses due to the oxygen diffuses to

263   and then adsorbs on catalyst surface to perform electrochemical reactions, which is determined by

264   both the electrode structure and the reactant provided, e.g. the mole fraction of oxygen against

265   nitrogen and water vapor in air at the cathode side. When the balance between diffusion and

266   consumption rates is achieved, a limit current density is reached. The formation of liquid water inside

267   the electrode void space restricts oxygen diffusion, especially if it is accumulated liquid water near the

268   downstream channel. However, the 2D model in this study failed to fully represent the whole MEA,

269   leading to an under-estimation of the impact of mass transfer losses in the downstream channel.

270   Especially for a large active area in the case of Wang [41], the departure of simulation result and

271 experimental data is more apparent.

3.2 Comparison of different mechanisms

273   Three models of describing the effect of liquid water generation were compared, based on the

274 polarization curves, through the reaction mechanism: traditional B-V, (1-s) corrected B-V and

275 agglomerate models. The results are shown in Fig. 4 and the channel lengths are 1 and 10 cm in Fig.

276 4(a) and Fig. 4(b), respectively. The current density predicted using (1-s) corrected B-V model was

277 slightly lower than that by traditional B-V model in the full range of cell voltage. Compared with Fig

278 3, we can see that the agglomerate model is in better agreement with the experimental results, while

279 the (1-s) corrected B-V model still shows limitations in describing the significant mass transport

280 resistance at high current density. This is because the cell performance at high current density is

281 determined by mass transport rather than electrochemical kinetics. Even through the predicted current

282 densities are deduced by considering the partial occupation of platinum active site by liquid water, the

283 (1-s) corrected B-V model fails to take the gas diffusion resistance through the ionomer film into

284 account. More rapid drop in current density was observed at high current densities in Fig. 4(b) in

285 comparison with that in Fig. 4(a), which indicated that the impact of mass transport on cell

286 performance at high current densities was more pronounced for long flow channels than for short

287 channels. This can be explained by the larger fuel concentration gradient and more liquid water

288 accumulation in the downstream channel. It is also clear, due to slow reaction rate and low mass

289 transport impact at low current densities, the results predicted by the agglomerate model were very

290 close to that of B-V model. However, the agglomerate model is capable of capturing the impact of

291 mass transport at high current densities by considering the species transport resistance through the

292 ionomer and liquid water films surrounding agglomerates.

3.3 Distributions of reactant gases

The mole fractions of hydrogen and oxygen within electrode and flow channel at various current densities from 0.2 to 1.4 A cm^{-2} are shown in Fig. 5. It is clear the concentrations of both hydrogen and oxygen decrease along the diffusion direction and the concentration gradient is more apparent at high current densities. Hydrogen consumption near the anode outlet is observed from the distribution of hydrogen mole fraction shown in Fig. 5(a). This can be explained by the electrochemical reaction and the effect of electro-osmotic drag (EOD), especially at high current densities. The increase in current density from 0.6 to 1.0 A cm^{-2} leads to a 69% increase in the rate of hydrogen consumption by HOR and a 63% increase in the water flux under the driving force of EOD. In comparison with hydrogen concentration distribution in flow channel, Fig. 5(b) indicates that, oxygen remains at a very high concentration close to the inlet level in flow channel, in the full range of current densities from 0.2 to 1.4 A cm^{-2}, along the air flow direction. On the contrary, a significant concentration gradient is shown through the diffusion direction as the current density increases, which is in consistence with the previous modelling results of Nguyen et al. [42]. This can be explained by the increase in oxygen consumption due to the accelerated ORR and the presence of large oxygen transport resistance through the electrode. In addition, the more water generated at high current density dilutes the oxygen. The formation of liquid water reduces the porosity of the electrode and increases the thickness of liquid water film surrounding the agglomerate, leading to a further decrease in the oxygen diffusivity through the electrode before it can reach the active sites. However this does not happen at the anode side due to the much easier diffusion of the smaller hydrogen molecular and its relative high mole fraction.

3.4 Distributions of effectiveness factor

315   The effectiveness factors, used to evaluate how effective the catalyst layer is utilized, of the ACL

316   and CCL at various current densities from 0.3 to 1.2 A cm^{-2} are shown in Fig. 6. In Fig. 6(a), X=0 and

317   X=1 represent the interfaces of GDL-CL and CL-membrane of anode, while Y=0 and Y=1 represent

318   the anode inlet and outlet, respectively. In Fig. 6(b), X=0 and X=1 represent the interfaces of

319   membrane-CL and CL-GDL of cathode, while Y=0 and Y=1 represent the cathode outlet and inlet,

320   respectively. The highest effectiveness factors, for both the ACL and CCL, are observed at 0.3 A cm^{-2},

321   which decrease with the increase of the current density to 1.2 A cm^{-2}. The decrease in effectiveness

322   factor can be explained by the increased electrochemical reaction rate as the current density increases.

323   At this stage, the overall reaction rate is mainly determined by the rate of chemical reaction rather

324   than mass transport. As the current density increases, the increase in electrochemical reaction rate

325   leads to a faster consumption of reactant gases relative to the diffusion rate to the active sites. The rate

326   determining process therefore changes from the electrochemical reaction to the reactant gas diffusion.

327   Consequently, along the gas diffusion direction through catalyst layers, the catalyst utilization is

328   higher near the GDL-CL interface (*X*=0 for anode and *X*=1 for cathode) than that of the CL-membrane

329   interface (*X*=1 for anode and *X*=0 for cathode), which agree with the finding of Sun et al. [26]. It is

330   important to note that the change of the effectiveness factor is not pronounced along the reactant gas

331   flow direction (*Y* direction). This is because the gases are supplied above stoichiometric requirements.

332   Reactant gases are provided at such rates to guarantee the almost uniform concentrations along the

333   channels. A comparison of Fig. 6(a) and Fig. 6(b) shows a much higher effectiveness factor of ACL

334   than that of CCL, especially at high current densities. The ACL effectiveness factor remains high, ca.

335   80%, for a certain distance along the hydrogen diffusion. On the contrary, due to the large oxygen

336   transport resistance through the cathode, the effectiveness factor of CCL is much lower compared

337 with that of ACL. The platinum catalyst in the CCL located near the CL-GDL interface cannot be

338 fully utilized, resulting in a waste of expensive catalyst.

3.5   Distributions of current density

340 Fig. 7 shows the current density distributions within the catalyst layers of anode and cathode at

341 various cell voltages from 0.7 to 0.4 V. The current densities increase in both catalyst layers as the cell

342 voltage decreases. It can be seen that the current densities decrease along the reactant gas diffusion

343 direction at both the anode and cathode, leading to insufficient utilization of the catalyst near the

344 CL-membrane boundary ($X=0$ for cathode and $X=1$ for anode). On the contrary, the current densities

345 almost remain constant along the reactant flow direction. It is apparent that the current density

346 distribution in the ACL is more uniform than that in the CCL. In the region near the CL-membrane

347 interface, the anode current density is higher than the cathode current density at a fixed cell voltage.

348 This can be explained by the sluggish ORR in the cathode. Due to the slower ORR in the cathode, the

349 interior of the cathode catalyst layer is not fully utilised, especially at a high current density.

3.6   Distributions of liquid water saturation

351 The liquid water saturations in both electrodes, including CLs and GDLs, are shown in Fig. 8. The

352 coordinates of X and Y indicate the same geometry as those in Fig. 6. It is clear that the liquid water

353 saturation increases in both electrodes as the current density increases. Also, the liquid water

354 saturation is relatively high near the outlets in both electrodes, indicating more severe water flooding

355 in these areas. This finding is in consistence with the experimental measurement of Iranzo et al. [20].

356 Comparison of Fig. 8(a) and Fig. 8(b) shows that the gradient of liquid water saturation is greater in

357 cathode electrode than of the anode, especially along the channel direction.

3.7   Distributions of temperature

359 The temperature profiles at various current densities from 0.6 to 1.0 A cm^{-2} are shown in Fig. 9. A

360 non-uniform temperature distribution is clearly indicated. The temperature increases along the air

361 flow and decreases from the cathode to the anode through the membrane with the highest value at the

362 cathode side. The most significant temperature rise, as expected, is observed in the cathode, leading to

363 a ca. 4 °C difference between anode and cathode at 1.0 A cm^{-2}. This temperature increase at the

364 cathode can be explained by both the exothermic ORR and water phase-transfer occurred. The latter

365 comprises ca. 6% of the total heat released at 1.0 A cm^{-2} (Table 7), which is the latent heat associated

366 with water phase change from dissolved water to liquid water during membrane/ionomer desorption.

367 A temperature rise along the cathode flow channel is clearly shown in Fig. 9. This can be explained by

368 the heat released by water phase-transfer as liquid water is pushed downstream to the channel exit by

369 the airflow.

370 As a main heat source, the heat released by ORR comprises more than 90% of the total heat

371 released at 1.0 A cm^{-2}. Similar to the ORR in the cathode, the HOR in the anode occupies more than

372 88% of the total heat change, which therefore can be considered as the main heat source in the anode.

373 Due to the endothermic nature and large contribution of the HOR to the total heat in the anode, the

374 anode is endothermic in full range of current densities. With the increase in current density, the ratio

375 of HOR to the total heat in the anode increases whereas that of ORR to the total heat in the cathode

376 decreases. In the anode, the heat released by ionomer water uptake is the second main heat source,

377 which comprises ca. 10% of the total heat in the anode at 0.2 A cm^{-2}. As the current density increases,

378 there is a decrease in the contribution of the heat released by ionomer water uptake in the anode. This

379 is caused by a relative fast increase in the heat absorption due to the HOR. Although the absolute heat

380 released by ionomer water uptake increases, the ratio decreases from ca. 11% to 3% as the current

381   density increases from 0.2 to 1.0 A cm^{-2}. Table 7 also shows that the heat contribution of ORR

382   decreases and ionomer desorption increases with the increase in current density in the cathode. This is

383   because more dissolved water is generated at a high current density, which then transfers to liquid

384   water by ionomer desorption after the ionomer is fully saturated.

385   The detailed temperature profiles at the anode channel-GDL interface are shown in Fig. 10. The

386   temperature increases sharply along the hydrogen flow direction until a maximum temperature is

387   achieved, then slightly decreases near the anode outlet. The maximum temperature is located in the

388   middle of the channel near to the inlet. The temperature rise in the anode is much less than that of the

389   cathode due to the endothermic HOR within the anode catalyst layer (Fig. 9). This increase can be

390   explained by the heat transferred from the cathode and the latent heat released via water phase-transfer.

391   As shown in Table 7, the heat via water phase-transfer approximately comprises 11% of total heat in

392   the anode at 0.2 A cm^{-2}, which decreases to less than 3% as the current density increases to 1.0 A cm^{-2}.

393   Therefore, heat transfer from the cathode is the main heat source contributed to the temperature rise in

394   the anode.

3.8   Comparison of the isothermal and non-isothermal model

396   Fig. 11 shows the liquid water saturation at the cathode CL-GDL interface at 1.0 A cm^{-2} simulated

397   by both the isothermal and non-isothermal models. The dimensionless coordinate is the same as in Fig.

398   1. The liquid water saturation increases along the air flowing direction at the cathode GDL-CL

399   interface. By taking the temperature rise into account, the liquid water saturation predicted by the

400   non-isothermal model is slightly smaller than that by the isothermal model, caused by the fast increase

401   in the saturation pressure of water vapour (p_{sat}) with temperature. Specifically, p_{sat} increases from

402   31.16 to 36.99 kPa as temperature increases from 70 to 74 °C. The increase in the saturation pressure

403   of water vapour, improves the water carrying capacity (WCC) of gas mixture, thus to a certain extent,

404   prohibits the water phase-transfer from vapour to liquid water. Furthermore, the temperature rise is

405   more apparent at a high operating temperature in comparison with a low one [38]. The heat released

406   during fuel cell operation can help mitigate water flooding by improving the WCC of the reactant

407   gases. However, this is at the expense of reducing the effective oxygen concentration of the cathode

408   reactant gas, which may results in a more significant decline in cell performance than that induced by

409   flooding. The mole fraction of oxygen in a fully humidified mixture decreases from 18.24% to 13.34%

410   as temperature increases from 70 to 74 °C, which may lead to oxygen starvation and damage to the

411   cathode. Thus, for a fuel cell operated at a high temperature, the performance may be limited by the

412   excessive moisture in the cathode reactant gas.

3.9   Regressed expressions for liquid water saturation

414   Fig. 12 shows the liquid water saturation in both electrodes (including CLs and GDLs) at various

415   current densities. It indicates that the increase of the current density leads to a logarithmic increase in

416   the liquid water saturation, which is greater in the cathode than that in the anode. In addition, the

417   liquid water saturations are slightly larger in CLs than that in GDLs at both electrodes, especially in

418   the cathode due to the water generated via ORR.

419   Mathematical expressions are regressed in terms of logarithmic and exponential equations to fit the

420   average liquid water saturation in both electrodes, as shown in Fig. 13, respectively. Linear

421   logarithmic transform function (Log3P1) and two-phase exponential decay function with time offset

422   (ExpDecay2) were selected as regression functions. The cathode average liquid water saturation (s_c) in

423   Fig. 13(a) could be well fitted by a logarithmic expression (Eq. 22) with a R^2 coefficient of 99.33%.

424   (R^2 is a statistical measure of how close the data to the fitted regression line). However, a large error

425   of fitting occurs in medium and high current densities when applying the same regression function to

426   the anode average liquid water saturation (s_a). The logarithmic expression (Eq. 23) led to a R^2

427   coefficient of only 94.26% and a remarkable standard error of parameter c. Thus, the logarithmic

428   expression of s_a - i was considered as an unconfident relationship without enough accuracy. Instead,

429   an exponential expression (Eq. 24), more complex in form in comparison with logarithmic expression,

430   is regressed in Fig. 13(b). It can be seen that the exponential express is more accurate here.

431    $$s_c = 0.1344 + 0.05912\ln(i+0.15109) \quad (R^2 > 99.33\%) \tag{22}$$

432    $$s_a = 0.07405 + 0.01354\ln(i+3.00567\times10^{-4}) \quad (R^2 > 94.26\%) \tag{23}$$

433    $$s_a = 0.10232 - 0.06965\exp(-\frac{i+0.00489}{1.12255}) - 0.0378\exp(-\frac{i+0.00489}{0.02805}) \quad (R^2 > 99.88) \tag{24}$$

434   The average liquid water saturations in both electrodes with respect to the current density higher

435   than 0.6 A cm^{-2} are shown in Fig. 14. Log3P1 function, which is used to fit the data plotted, results in

436   accurate expressions (Eq. 25 and Eq. 26) with R^2 greater than 99.9% in both electrodes. This indicates

437   that the changes in the average liquid water saturation in both electrodes follows a logarithmic

438   relationship at current densities higher than 0.6 A cm^{-2}. Comparing Fig. 14 with Fig. 13(b) suggests

439   that, as the current density increases, the increase in the average liquid water saturation in the anode

440   firstly obeys exponential function at low current densities followed by logarithmic function at high

441   current densities. However, it is insufficient to describe the relationship between the anode average

442   liquid water saturation and current density using a logarithmic function in full range of current

443   densities.

444    $$s_c = 0.11463 + 0.07763\ln(i+0.40119) \quad (R^2 > 99.99\%) \tag{25}$$

445    $$s_a = 0.06909 + 0.02897\ln(i+0.16568) \quad (R^2 > 99.90\%) \tag{26}$$

446   The relationship between average liquid water saturation in the anode and the cathode is regressed

447 in Fig. 15. The data plotted can be roughly divided into three segments, corresponding to the liquid

448 water saturation at the low, medium and high levels. In order to guarantee the accuracy, the R^2

449 coefficient of each regression expression within each segment is controlled greater than 99.9%. The

450 results indicate that at the low and high liquid water saturation, a linear relationship exists between the

451 average liquid water saturations in the anode and the cathode. However, at the medium liquid water

452 saturation, the exponential function is more accurate than the linear relationship. The relation of liquid

453 water saturation at the anode and cathode is similar to the modelling results of Jiang and Wang [43].

454 As stated by O'Rourke et al. [21], the water flooding in anode could be detected prior to severe

455 damage of cathode catalyst, which could be avoided with the aid of the regressed expressions of the

456 liquid water saturation in the anode and the cathode.

457 $$s_c = 3.65764s_a - 1.45542 \times 10^{-4} \quad (R^2 > 99.99\%) \quad \text{low water saturation} \tag{27}$$

458 $$s_c = \exp(27.0888s_a^2 + 31.24035s_a - 4.00174) \quad (R^2 > 99.44\%) \quad \text{medium water saturation} \tag{28}$$

459 $$s_c = 2.32873s_a - 0.03044 \quad (R^2 > 99.96\%) \quad \text{high water saturation} \tag{29}$$

4. Conclusion

461 A two-dimensional, two-phase flow, along-the-channel, non-isothermal, CFD model for a single

462 PEMFC is developed. Water was treated as three different phases: vapour, dissolved and liquid water.

463 The water phase-transfer between each phase, associated with the combinational transport mechanism

464 through the membrane, is numerically studied. Three types of models are compared for hydrogen

465 reduction and oxygen oxidation in catalyst layers, including traditional B-V, (1-s) corrected B-V and

466 agglomerate mechanism. Temperature changes in MEA and channels due to electrochemical reaction,

467 ohmic resistance and water phase change are analysed and the contribution of each heat source is

468 summarised and compared at a variety of current densities. Mathematical expressions for liquid water

469   saturations against current density at both anode and cathode are regressed and the mathematical

470   relationship between them is developed. Analysis of the simulation results leads to the following

471   insights:

472   The current density predicted by traditional B-V, (1-s) corrected B-V and agglomerate models are

473   in general agreement with experimental data at low current densities. As the current density increases,

474   by accounting for the extra oxygen diffusion resistance through the ionomer/water film and the loss of

475   catalyst layer porosity due to ionomer swelling, the agglomerate model gives more accurate

476   simulation results in comparison with the others. However, due to significant water flooding in

477   downstream channel, the 2D model developed cannot fit the experimental data very well at high

478   current densities, especially when long flow channels are applied. Due to the more significant

479   transport resistance of oxygen in the cathode than that of hydrogen in the anode, the effectiveness

480   factor of the cathode catalyst layer is much lower than that of the anode catalyst layer.

481   Water flooding, represented by the liquid water saturation, is prone to occur near the downstream

482   channel of both the anode and cathode. Liquid water saturation is temperature dependent, which

483   requires the non-uniform distribution of temperature predicted by the non-isothermal model. The most

484   significant temperature rise is in the cathode catalyst layer due to the contribution of exothermic ORR,

485   which comprises more than 90% of total heat released. With the increase in the current density, the

486   heat contribution of ORR decreases while ionomer/membrane desorption increases. On the contrary,

487   the endothermic HOR is the main heat source in the anode. At a low current density, the heat released

488   by ionomer/membrane water uptake contributes ca. 10% to the total heat in the anode.

489   The mathematical expressions for the relationship between the current density and liquid water

490   saturations in both the anode and the cathode are regressed. Nonlinear current density – water

491   saturation relations are found at both electrodes. It is believed that the liquid water saturation in the

492   cathode presents logarithm relevant to current density. However, the liquid water saturation in the

493   anode increases exponentially as the current density increase. At a high current density greater than

494   0.6 A cm^{-2}, the liquid water saturations at both electrodes can be described by logarithmic relationship.

495   The relationship between liquid water saturations in the anode and the cathode is also regressed. It is

496   found that at low and high current densities, the relationship can be accurately represented by linear

497   function, but exponential function is believed to be more accurate at medium current densities.

Acknowledgements

References

502   [1]   Gottesfeld S. Fuel cell techno-personal milestones 1984-2006. J Power Sources 2007;171:37-45.

503   [2]   Dai W, Wang H, Yuan XZ, Martin JJ, Yang D, Qiao J, Ma J. A review on water balance in the
504   membrane electrode assembly of proton exchange membrane fuel cells. Int J Hydrogen Energy
505   2009;34:9461-78.

506   [3]   Wang Y, Chen KS, Mishler J, Cho SC, Adroher XC. A review of polymer electrolyte membrane
507   fuel cells: Technology, applications, and needs on fundamental research. App Energy
508   2011;88:981-1007.

509   [4]   Wang J. Barriers of scaling-up fuel cells: Cost, durability and reliability. Energy 2015;80:509-21.

510   [5]   Lund H, Andersen AN, Østergaard PA, Mathiesen BV, Connolly D. From electricity smart grids
511   to smart energy systems – A market operation based approach and understanding. Energy
512   2012;42:96-102.

513   [6]   Rokni M. Thermodynamic and thermoeconomic analysis of a system with biomass gasification,
514   solid oxide fuel cell (SOFC) and Stirling engine. Energy 2014;76:19-31.

515   [7]   Cappa F, Facci AL, Ubertini S. Proton exchange membrane fuel cell for cooperating households:

516   A convenient combined heat and power solution for residential applications. Energy

517   2015;90:1229-38.

518   [8] Carton JG, Olabi AG. Wind/hydrogen hybrid systems: Opportunity for Ireland's wind resource to

519   provide consistent sustainable energy supply. Energy 2010;35:4536-44.

520   [9] Djilali N. Computational modelling of polymer electrolyte membrane (PEM) fuel cells:

521   Challenges and opportunities. Energy 2007;32:269-80.

522   [10]   Bazylak A. Liquid water visualization in PEM fuel cells: A review. Int J Hydrogen Energy

523   2009;34:3845-57.

524   [11]   Carton JG, Lawlor V, Olabi AG, Hochenauer C. Zauner G. Water droplet accumulation and

525   motion in PEM (Proton Exchange Membrane) fuel cell mini-channels. Energy 2012;39:63-73.

526   [12] Ge S, Li X, Yi B, Hsing IM. Absorption, desorption, and transport of water in polymer electrolyte

527   membranes for fuel cells. J Electrochem Soc 2005;152:A1149-57.

528   [13] Wu H, Berg P, Li X. Steady and unsteady 3D non-isothermal modeling of PEM fuel cells with

529   the effect of non-equilibrium phase transfer. App Energy 2010;87:2778-84.

530   [14] Yang XG, Ye Q, Cheng P. Matching of water and temperature fields in proton exchange

531   membrane fuel cells with non-uniform distributions. Int J Hydrogen Energy 2011;36:12524-37.

532   [15] Djilali N. Computational modelling of polymer electrolyte membrane (PEM) fuel cells:

533   Challenges and opportunities. Energy 2007;32:269-80.

534   [16] Das PK, Li X, Liu ZS. Analysis of liquid water transport in cathode catalyst layer of PEM fuel

535   cells. Int J Hydrogen Energy 2010;35:2403-16.

536   [17] Meng H, Wang CY. Model of Two-Phase Flow and Flooding Dynamics in Polymer Electrolyte

537   Fuel Cells. J Electrochem Soc 2005;152:A1733-41.

538   [18] Ferreira RB, Falcao DS, Oliveira VB, Pinto AMFR. Numerical simulation of two-phase flow in

539   an anode gas channel of a proton exchange membrane fuel cell. Energy 2015;82:619-28.

540   [19] Wong KH, Loo KH, Lai YM, Tan SC, Tse CK. A theoretical study of inlet relative humidity

541   control in PEM fuel cell. Int J Hydrogen Energy 2011;36:11871-85.

542 [20] Iranzo A, Boillat P, Biesdorf J, Salva A. Investigation of the liquid water distribution in a 50 cm2

543   PEM fuel cell: Effects of reactants relative humidity, current density, and cathode stoichiometry.

544   Energy 2015;82:914-21.

545 [21] O'Rourke J, Ramani M, Arcak M. In situ detection of anode flooding of a PEM fuel cell. Int J

546   Hydrogen Energy 2009;34:6765-70.

547 [22] Anderson R, Blanco M, Bi X, Wilkinson DP. Anode water removal and cathode gas diffusion

548   layer flooding in a proton exchange membrane fuel cell. Int J Hydrogen Energy 2012;37:

549   16093-103.

550 [23] Wang ZH, Wang CY, Chen KS. Two-phase flow and transport in the air cathode of proton

551   exchange membrane fuel cells. J Power Sources 2001;94:40-50.

552 [24] He G, Ming P, Zhao Z, Abudula A, Xiao Y. A two-fluid model for two-phase flow in PEMFCs. J

553   Power Sources 2007;163:864-73.

554 [25] Ferreira RB, Falcao DS, Oliveira VB, Pinto AMFR. A one-dimensional and two-phase flow

555   model of a proton exchange membrane fuel cell. J Chem Technol Biotechnol 2015; 90:1547-51.

556 [26] Sun W, Peppley BA, Karan K. An improved two-dimensional agglomerate cathode model to

557   study the influence of catalyst layer structural parameters. Electrochim Acta 2005;50:3359-74.

558 [27] Shah AA, Kim GS, Sui PC, Harvey D. Transient non-isothermal model of a polymer electrolyte

559   fuel cell. J Power Sources 2007;163:793-806.

560 [28] Ju H, Meng H, Wang CY. A single-phase, non-isothermal model for PEM fuel cells. International

561   J Heat and Mass Transfer 2005;48:1303-15.

562 [29] Wang MH, Guo H, Ma CF. Temperature distribution on MEA surface of a PEMFC with

563   serpentine channel flow bed. J Power Sources 2006;157:181-7.

564 [30] Zhang GS, Guo LJ, Ma LZ, Liu HT. Simultaneous measurement of current and temperature

565   distributions in a proton exchange membrane fuel cell. J Power Sources 2010;195:3597-604.

566 [31] Lin H, Cao TF, Chen L, He YL, Tao WQ. In situ measurement of temperature distribution within

567   a single polymer electrolyte membrane fuel cell. Int J Hydrogen Energy 2012;37:11871-86.

568   [32] Pasaogullari U, Wang CY. Two-phase transport and the role of microporous layer in polymer

569   electrolyte fuel cells. Electrochim Acta 2004;49:4359-69.

570   [33] Wu H, Berg P, Li X. Modelling of PEMFC transients with finite-rate phase transfer processes. J

571   Electrochem Soc 2010;157:B1-12.

572   [34] Wang CY, Groll M, Rosler JS, Tu CJ. Porous medium model for two-phase flow in mini channels

573   with applications to micro heat pipes. Heat Recovery Syst CHP 1994;14:377-90.

574   [35] Xing L, Mamlouk M, Scott K. A two dimensional agglomerate model for a proton exchange

575   membrane fuel cell. Energy, 2013;61:196-210.

576   [36] Xing L, Song X, Scott K, Picker V, Cao W. Multi-variable optimization of PEMFC cathodes

577   based on surrogate modelling. Int J Hydrogen Energy 2013;38:14295-313.

578   [37] Xing L, Mamlouk M, Kumar R, Scott K. Numerical investigation of the optimal Nafion®

579   ionomer content in cathode catalyst layer: An agglomerate two-phase flow modelling. Int J

580   Hydrogen Energy 2014;39:9087-104.

581   [38] Xing L, Liu X, Alaje T, Kumar R, Mamlouk M, Scott K. A two-phase flow and non-isothermal

582   agglomerate model for a proton exchange membrane (PEM) fuel cell. Energy 2014;73:618-34.

583   [39] Xing L, Das PK, Song X, Mamlouk M, Scott K. Numerical analysis of the optimum

584   membrane/ionomer water content of PEMFCs: The interaction of Nafion® ionomer content and

585   cathode relative humidity. Appl Energy 2014;138:242-57.

586   [40] Barbir F. PEM fuel cells: theory and practice. 1st ed. Oxford: Elsevier Academic Press; 2005.

587   [41] Wang L, Husar A, Zhou T, Liu H. A parametric study of PEM fuel cell performances. Int J

588   Hydrogen Energy 2003;28:1263-72.

589   [42] Nguyen PT, Berning T, Djilali N. Computational model of a PEM fuel cell with serpentine gas

590   flow channels. J. Power Sources 2004;130:149-57.

591   [43] Jiang F, Wang C-Y. Numerical modeling of liquid water motion in a polymer electrolyte fuel cell.

592   Int J Hydrogen Energy 2014;39:942-50.

Nomenclature

A_s reaction surface area per unit platinum mass, $m^2\ kg^{-1}$

a specific area, m^{-1}

$c_{p,i}$ specific heat capacity of species i, $J\ mol^{-1}\ K^{-1}$

c concentration, $mol\ m^{-3}$

D diffusivity, $m^2\ s^{-1}$

D_c capillary diffusion coefficient, $m^2\ s^{-1}$

D_{ij} Maxwell-Stefan diffusion coefficient matrix, $m^2\ s^{-1}$

E effectiveness factor

E^0 open circle potential, V

E_{cell} cell voltage, V

EW equivalent weight of Nafion® membrane, $g\ mol^{-1}$

F Farady's constant, $96485\ C\ mol^{-1}$

f platinum mass ratio to Pt/C

H Henry's constant, $Pa\ m^3\ mol^{-1}$

i current density, $A\ m^{-2}$

i_0 exchange current density, $A\ m^{-2}$

$J(s)$ Leverett function

k rate coefficient, s^{-1}

k_i Thermal conductivity of species i, $W\ m^{-1}\ K^{-1}$

k_r relative permeability

k_p hydraulic permeability, m^2

l	thickness, m
L	volume fraction
M_j	molecular weight for specie j, kg mol^{-1}
M_T	Thieles's modulus
m	mass loading, mg cm^{-2}
N	number per volume, m^{-3}
n	number
p	pressure, Pa
R	ideal gas constant, 8.314 J mol^{-1} K^{-1}
R_M	membrane resistance, Ω m^{-2}
RH	relative humidity
r	radius, m
S	source term
s	liquid water saturation
T	temperature, K
$\mathbf{u}$	velocity vector, m s^{-1}
V	mole volume, m^3
w	mass fraction
X	normalised distance (x/δ_{CL})
x	mole fraction
Y	normalised distance ($z/(z_{CC}+z_{Ch})$)
$\%M$	volume fraction of primary pores occupied by ionomer

594

595   *Greek*

α charge transfer coefficient

α_w water activity

λ water content

μ viscosity, Pa s

ρ density, kg m^{-3}

ε porosity

δ thickness of ionomer/liquid water coating, m

γ oxygen diffusion rate through the coating, s^{-1}

η overpotential, V

σ surface tension, N m^{-1}

θ_c contact angel, °

σ_s electronic conductivity, S m^{-1}

σ_M ionic conductivity, S m^{-1}

φ potential, V

Ψ_w association parameter for water (the value is 2.6)

596   *Superscripts*

0   intrinsic

d   dissolved

eff   effective

ref   reference

eq		equilibrium
l		liquid
g		gas
597	*Subscripts*	
	a	anode
	ads	adsorption
	agg	agglomerate
	C	carbon
	c	cathode
	CL	catalyst layer
	des	desorption
	GDL	gas diffusion layer
	i	species i
	j	species j
	Kn	Knudsen diffusion
	M	Membrane/ionomer
	P	void space
	Pt	platinum
	Pt/C	platinum dispersed carbon
	p	primary pores
	r	relative
	S	GDL penetration

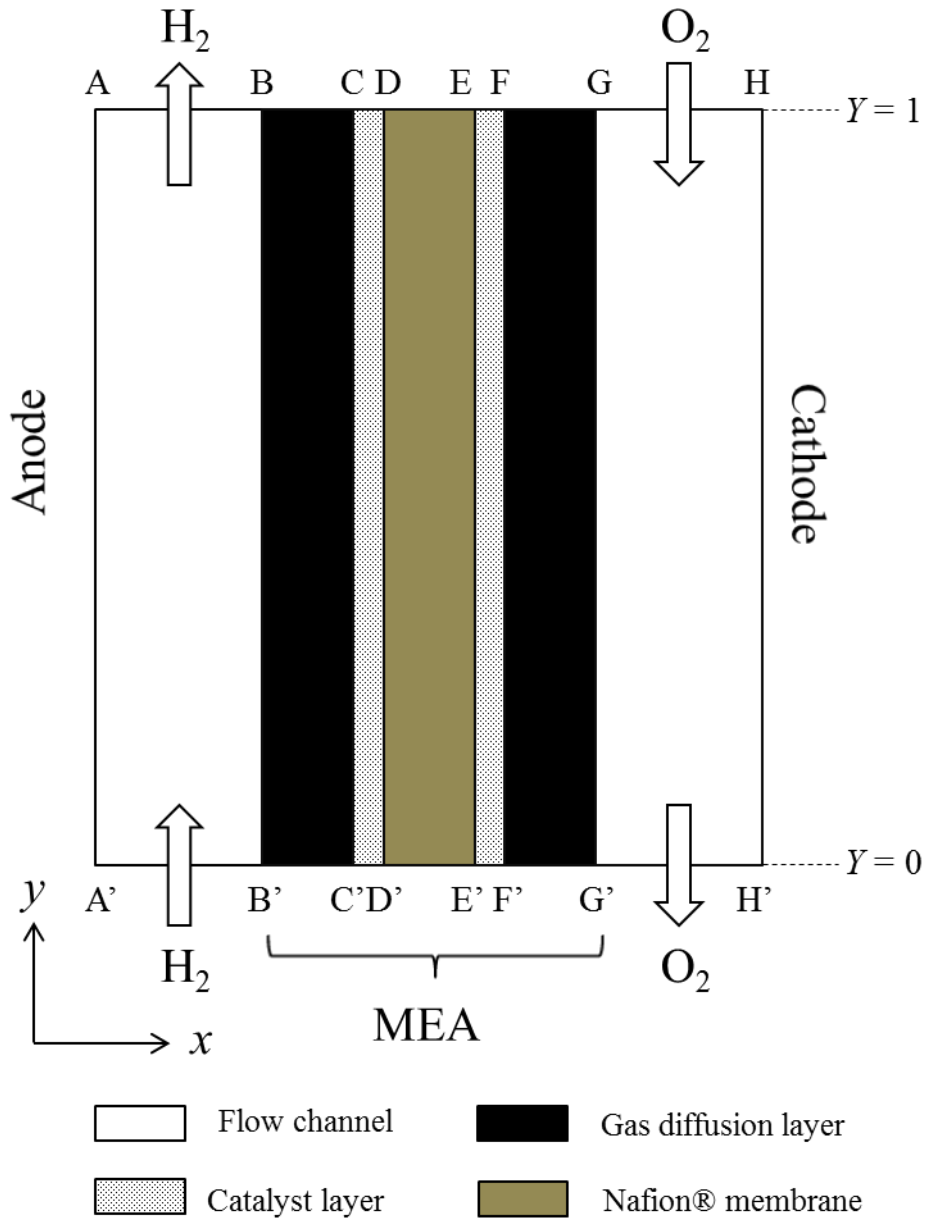|	
s	secondary pores
T	temperature
w	liquid water
sat	saturation
tot	total
vl	vapour to liquid
vd	vapour to dissolved
dl	dissolved to liquid

598

599

Fig. 1 Schematic of PEMFC unit and modelling domain: A-A' - anode flow channel outer boundary; B-B' - anode flow channel-GDL interface; C-C' - anode GDL-CL interface; D-D' – anode CL-membrane interface; E-E' - cathode CL-membrane interface; F-F' - cathode GDL-CL interface; G-G' – cathode flow channel-GDL interface; H-H' – cathode flow channel outer boundary
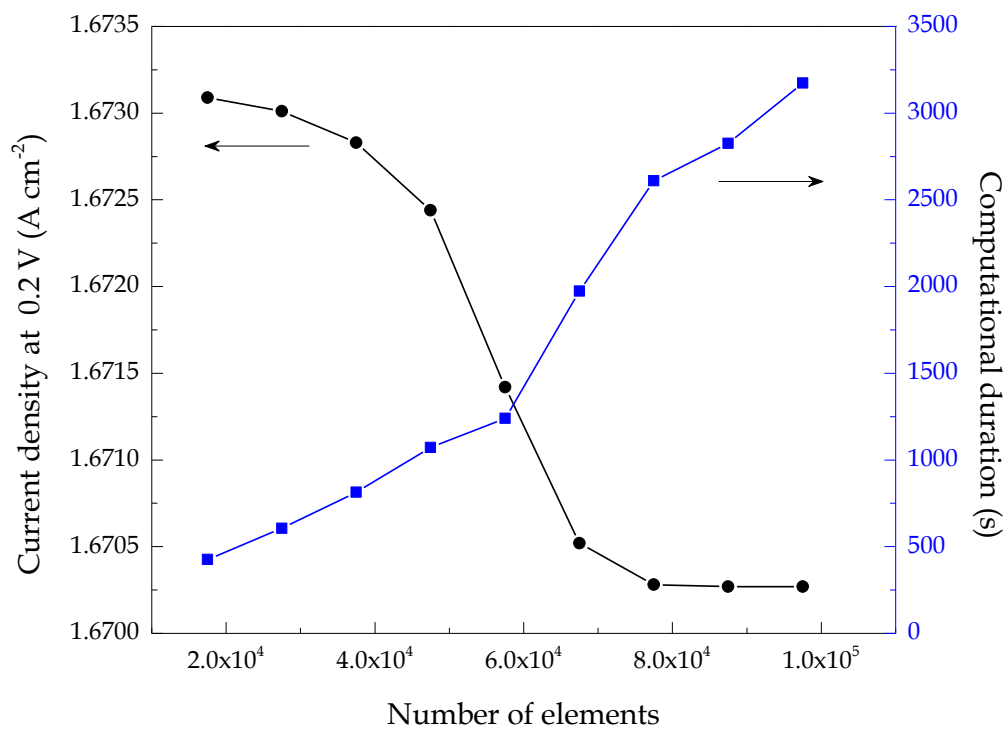
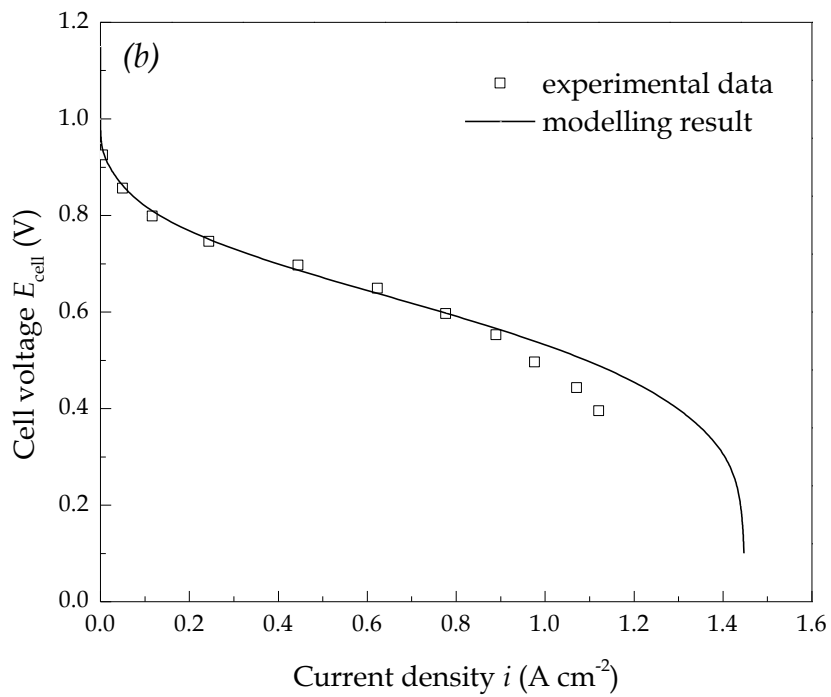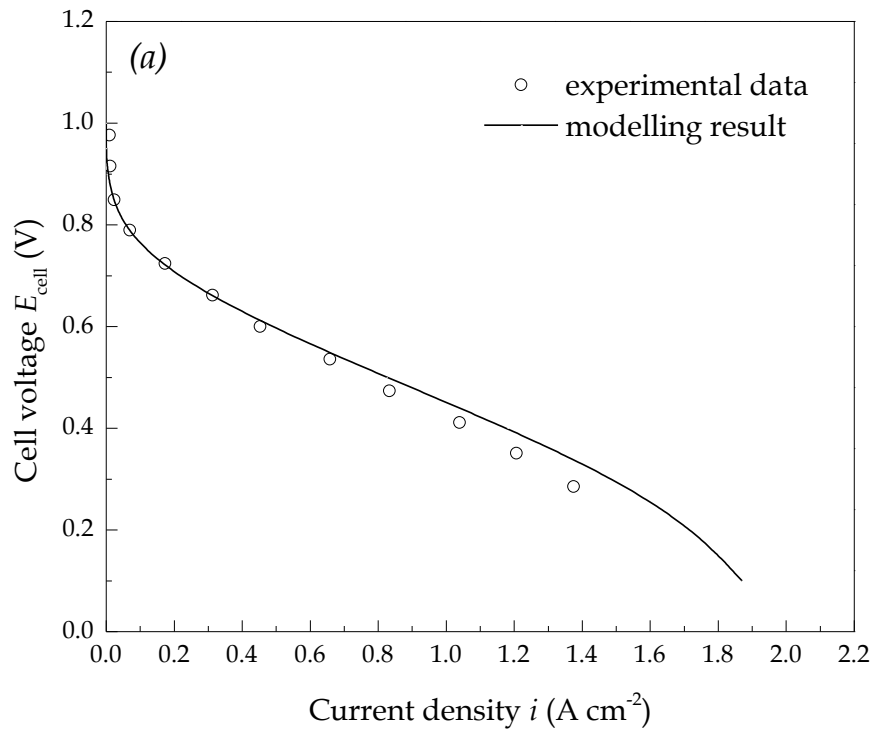Fig. 2 Effect of mesh characteristics on the current density at 0.2 V

612

613

614

615

616

617

618

619   Fig.3 Comparison between the modelling results and experimental data for two cases (a) 80 °C, 20% Pt/C, $m_{Pt,a} = 0.1$ mg

620   cm^{-2}, $m_{Pt,c} = 0.4$ mg cm^{-2},   effective area: 1.0 cm × 1.0 cm; (b) 70 °C, 40% Pt/C, $m_{Pt} = 0.4$ mg cm^{-2}, effective area: 7.2 cm ×

621   7.2 cm
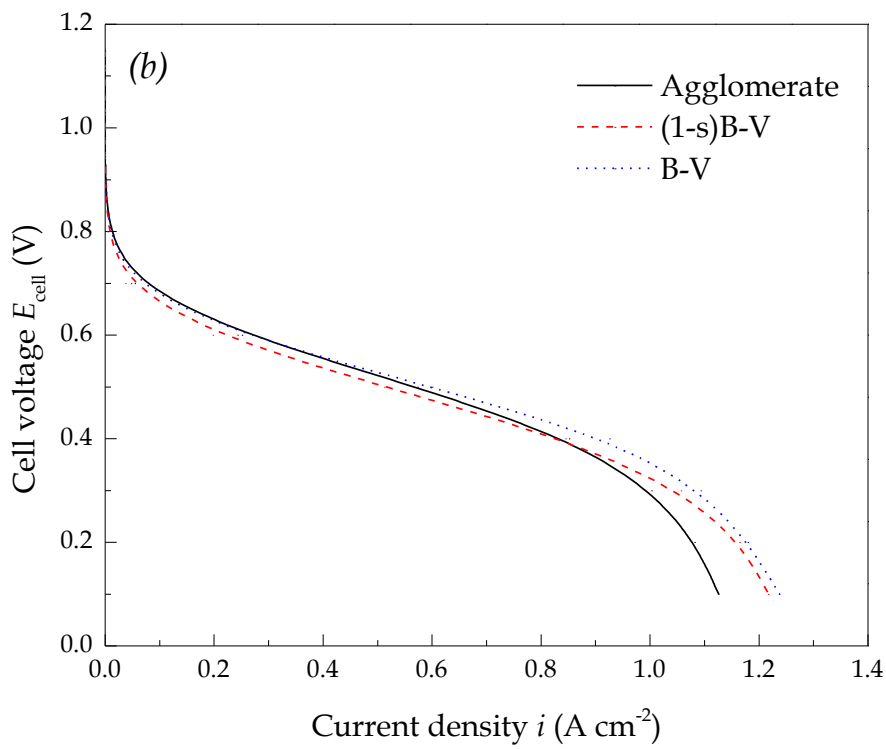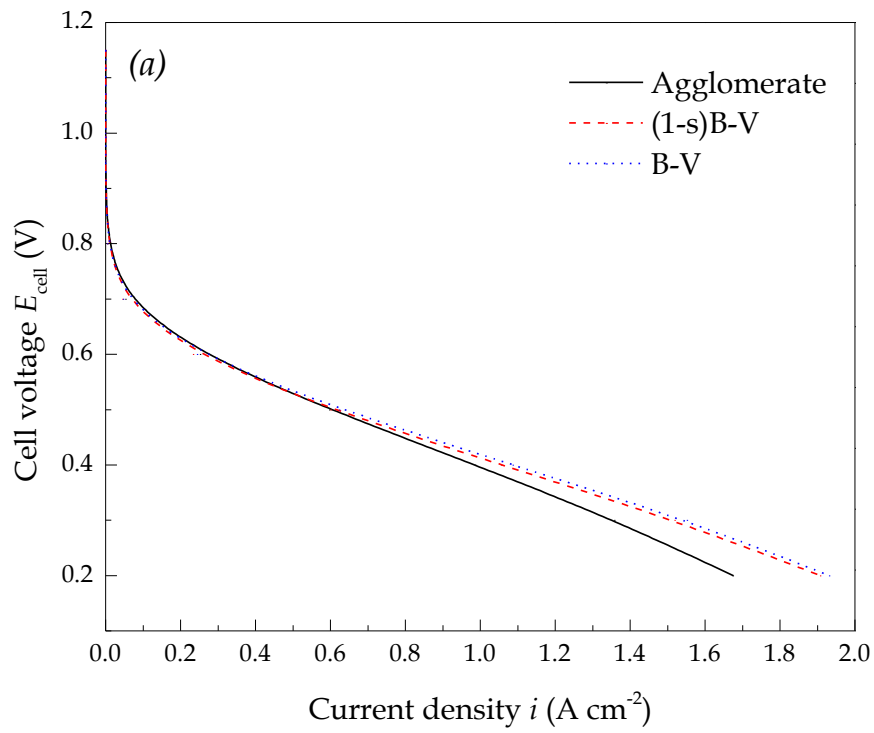
622

623
624　　　　　　Fig.4 Comparison of three mechanisms for (a) a short　1 cm channel and (b) a long 10 cm channel
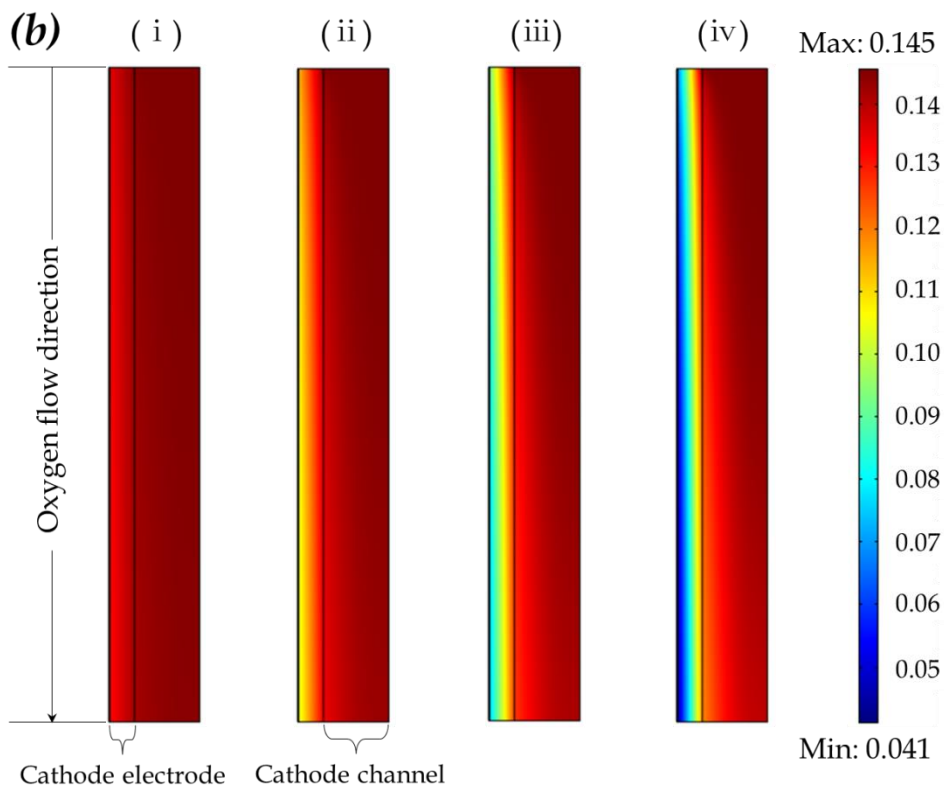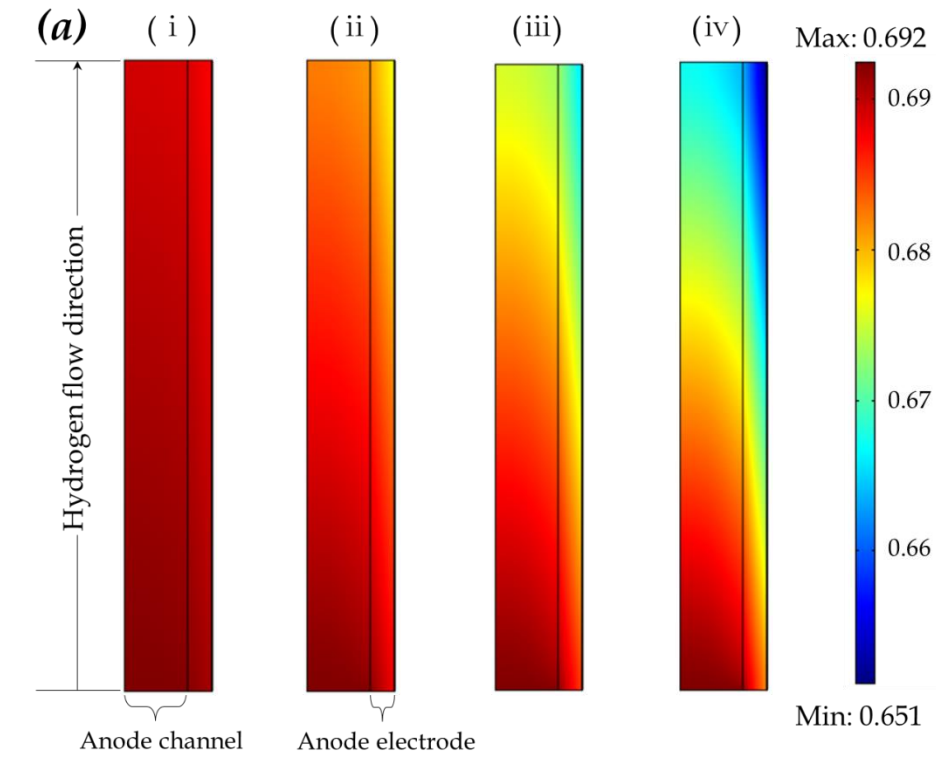
625

626
627

628   Fig.5 Distribution of mole fractions of (a) hydrogen and (b) oxygen at various current densities at (ⅰ) 0.2, (ii) 0.6, (iii) 1.0

629   and (iv) 1.4 A cm^{-2}

630

631

632
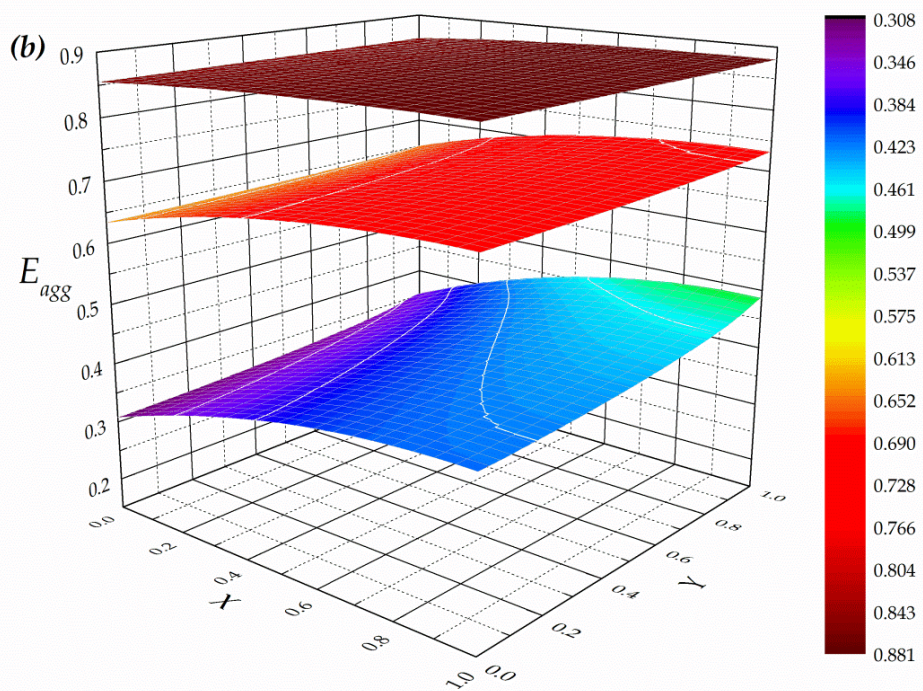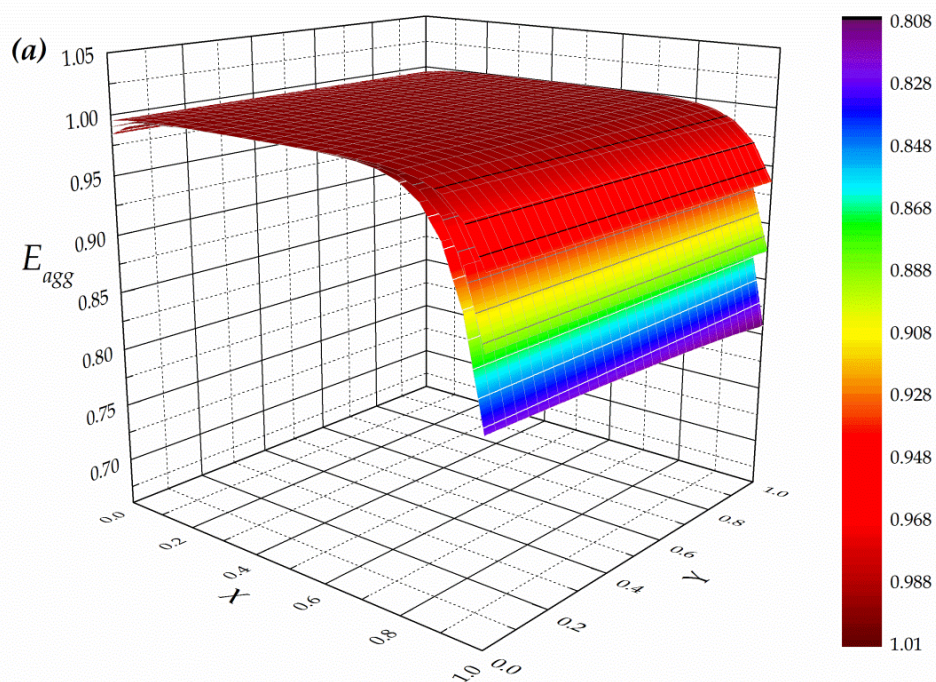
Fig.6 Effectiveness factor of (a) anode CL and (b) cathode CL at various current densities (from up down: 0.3, 0.7 and 1.2 A cm^{-2})

633

634

635

636
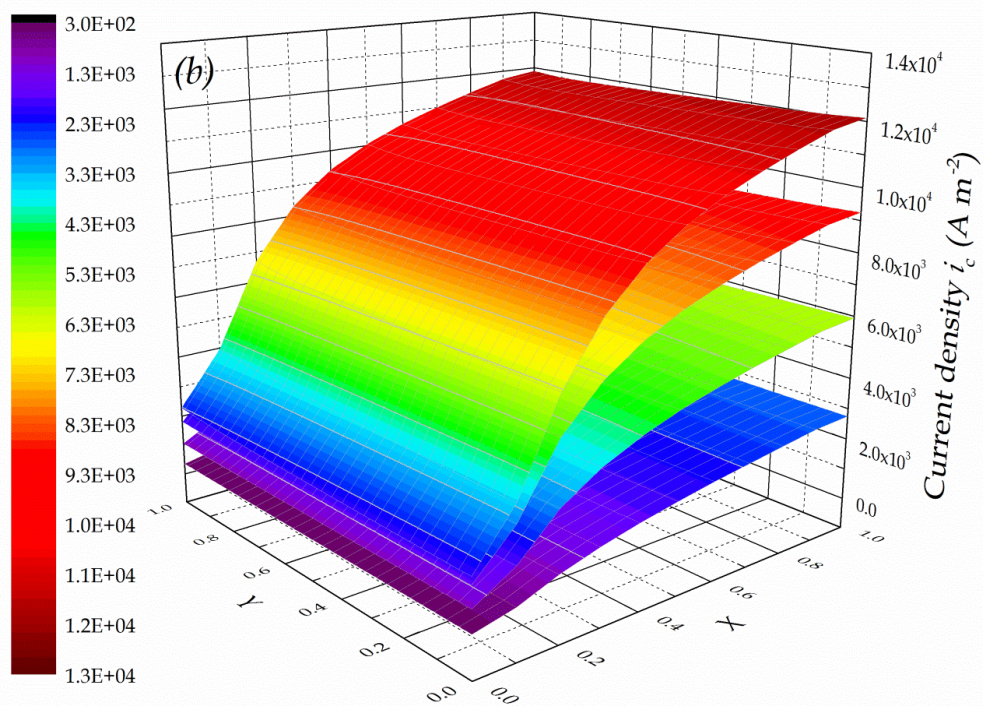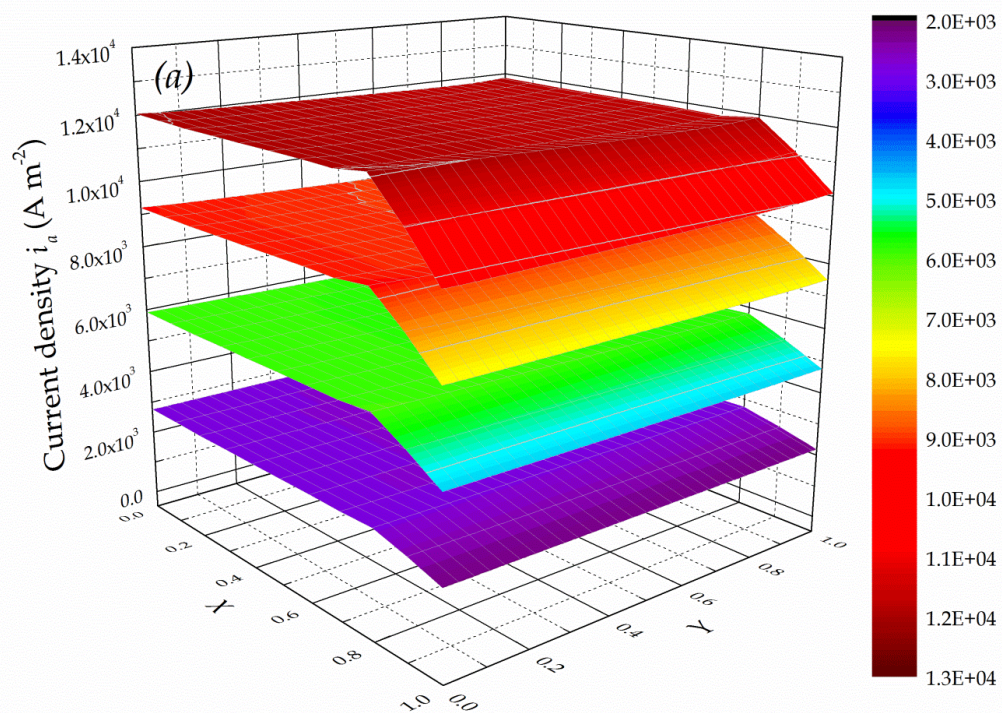
637
638
639   Fig. 7 Current density distribution within (a) the anode CL and (b) the cathode CL (from top down 0.7, 0.6, 0.5 and 0.4 V)
640
641
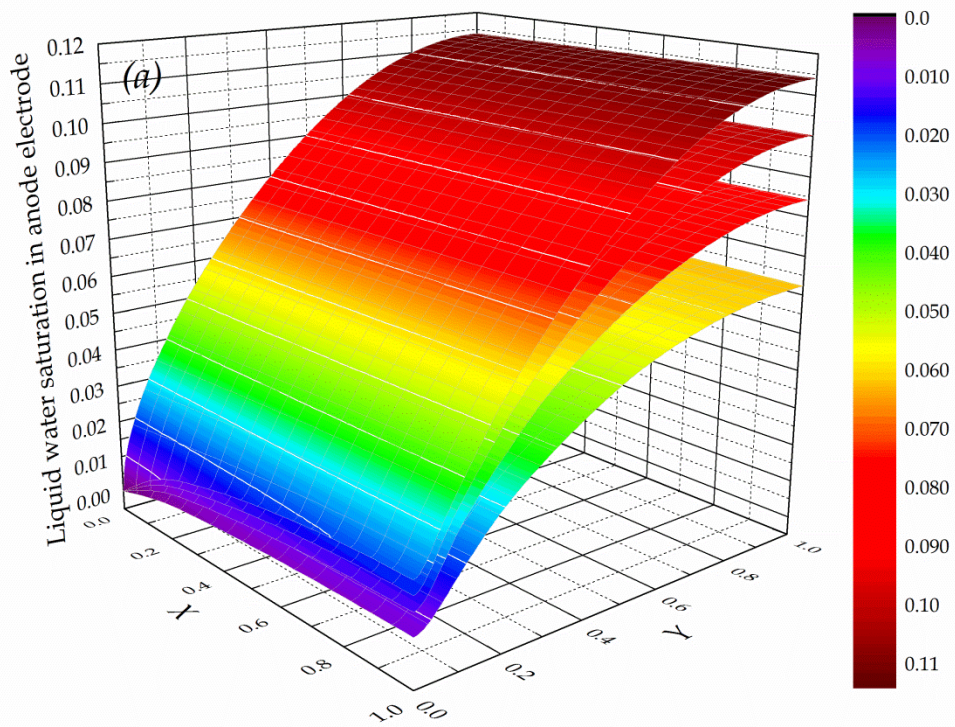
642
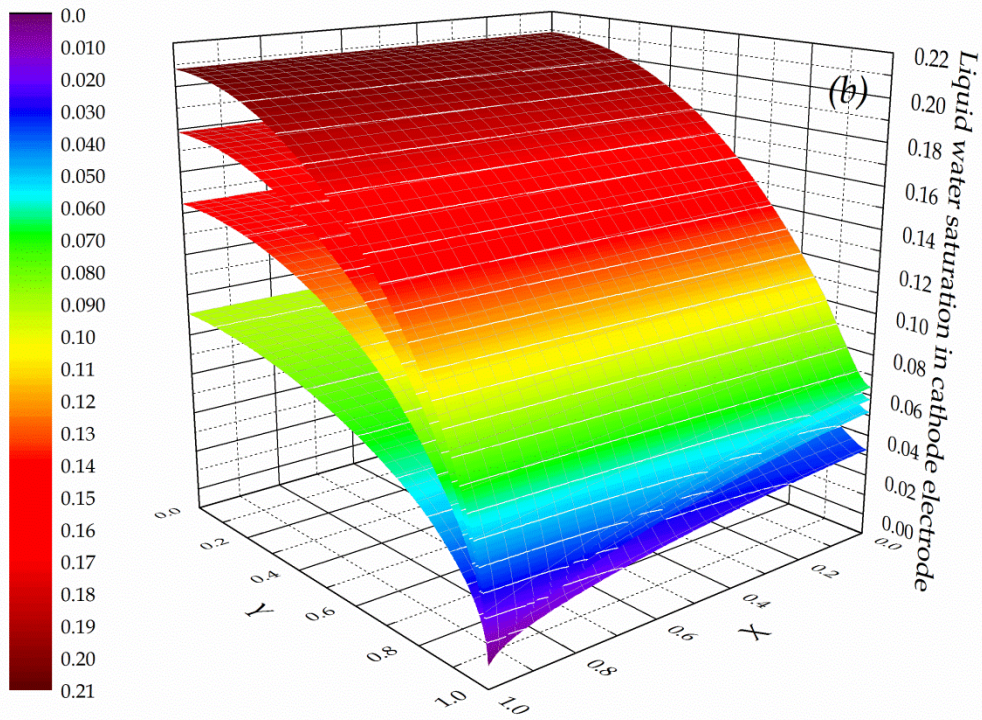
643

644   Fig.8 Liquid water saturation in CLs and GDLs of (a) anode and (b) cathode at various current densities (i = 0.2, 0.6, 1.0 and

645   1.4 A cm^{-2} from down up)
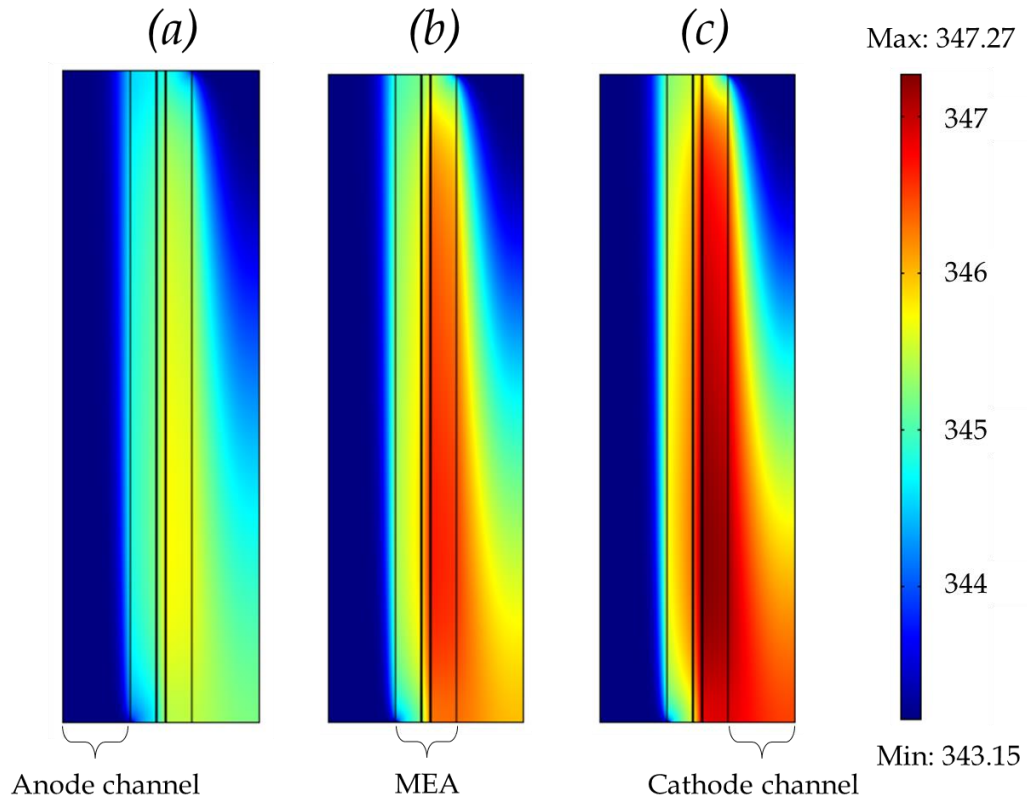
Fig.9 Temperature profiles at various current densities at (a) 0.6, (b) 0.8 and (c) 1.0 A cm^{-2}
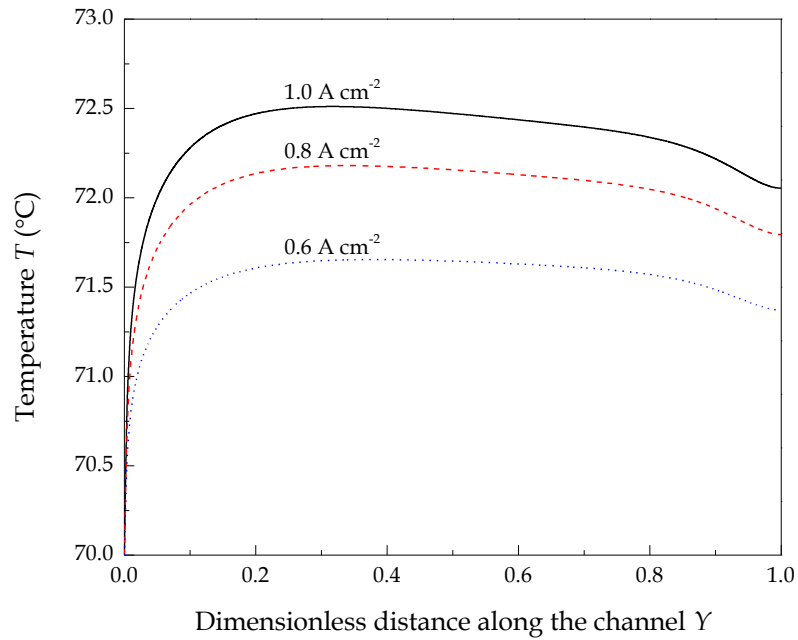
Fig.10 Detailed temperature profiles at anode channel-GDL interface at various current densities at (a) 0.6, (b) 0.8 and (c) 1.0 A cm^{-2}

652
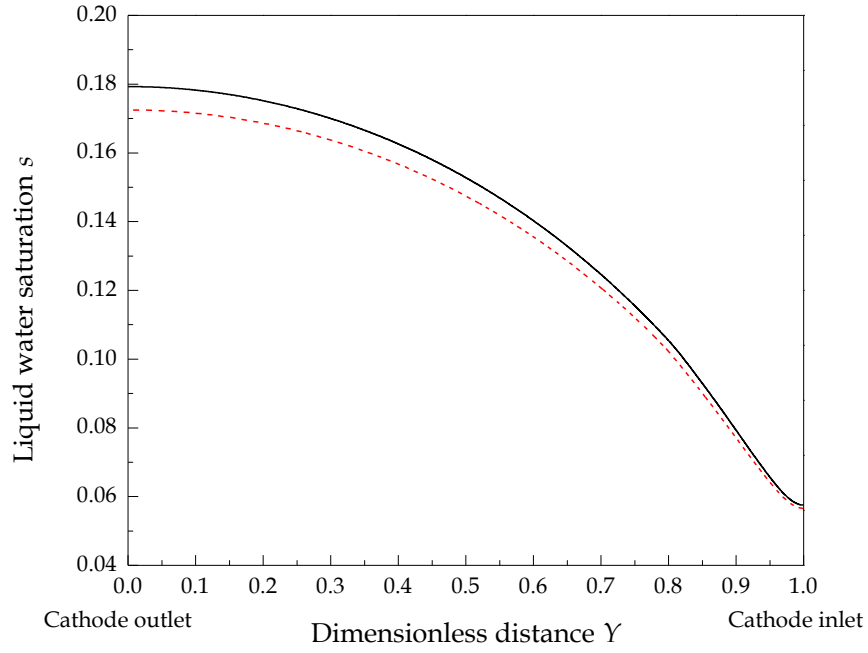
653   Fig. 11 Comparison of liquid water saturation at the cathode CL-GDL interface at 1.0 A cm^{-2}, predicted by isothermal and

654   non-isothermal models; Solid line - isothermal model prediction, Dash line - non-isothermal model prediction.

655

656
657
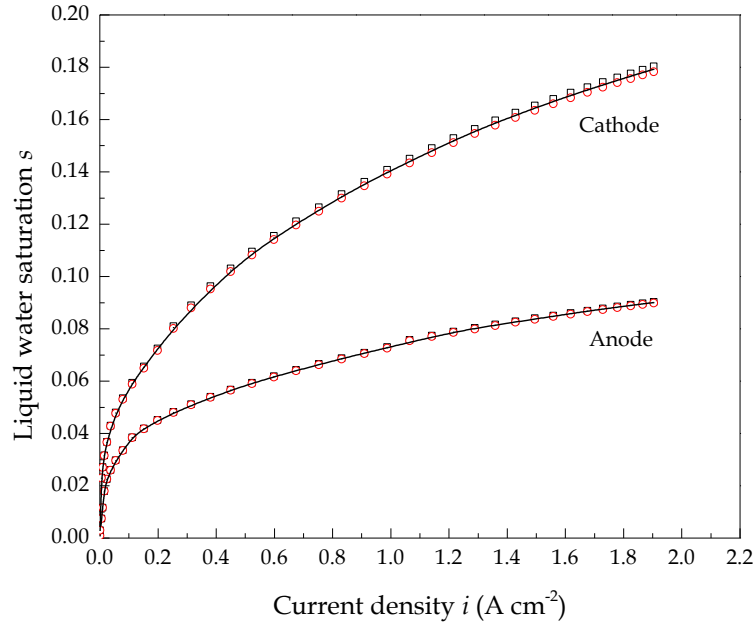
658   Fig. 12 Average liquid water saturation in both electrodes at various current densities: □- in catalyst layer, ○- in gas diffusion

659   layer, solid line – average value of CLs and GDLs

660

(a)

Average liquid water saturation in cathode s_c

Model	Log3P1		
Equation	$y = a - b*\ln(x+c)$		
Reduced Chi-Sqr	1.97278E-5		
Adj. R-Square	0.99329		
		Value	Standard Error
	a	0.1344	0.00192
B	b	-0.05912	0.0028
	c	0.15109	0.0211

Current density i (A cm^{-2})

661

(b)

Average liquid water saturation in anode s_a

Model	Log3P1		
Equation	$y = a - b*\ln(x+c)$		
Reduced Chi-Sqr	4.02939E-5		
Adj. R-Square	0.94262		
		Value	Standard Error
	a	0.07405	0.00121
B	b	-0.01354	7.2056E-4
	c	3.00567E-4	5.53822E-4

Model	ExpDecay2		
Equation	$y = y0 + A1*\exp(-(x-x0)/t1) + A2*\exp(-(x-x0)/t2)$		
Reduced Chi-Sqr	8.74111E-7		
Adj. R-Square	0.99876		
		Value	Standard Error
	y0	0.10232	0.00173
	x0	-0.00489	--
	A1	-0.06965	--
B	t1	1.12255	0.06379
	A2	-0.0378	--
	t2	0.02805	0.00203

Current density i (A cm^{-2})

662 Fig. 13 Regression expressions of the liquid water saturation versus current density in (a) cathode (b) anode; △-average

663 liquid water saturation, solid line - Log3P1 function fitted, dash line: ExpDecay2 function fitted.

664

Model	Log3P1	
Equation	y = a - b*ln(x+ c)	
Reduced Chi-Sqr	2.36427E-8	
Adj. R-Square	0.99994	
		Value	Standard Error
	a	0.11463	0.0017
B	b	-0.07763	0.00117
	c	0.40119	0.02297

Model	Log3P1	
Equation	y = a - b*ln(x+ c)	
Reduced Chi-Sqr	7.83812E-8	
Adj. R-Square	0.99901	
		Value	Standard Error
	a	0.06909	0.00192
D	b	-0.02897	0.0015
	c	0.16568	0.0653

665

666

667   Fig. 14 Regression expressions of the average liquid water saturation in both electrodes versus current density at the current

668   density > 0.6 A cm^{-2}, □- in anode electrode,○- in cathode electrode, solid lines - Log3P1 function fitted

The figure contains the following fitted data boxes:

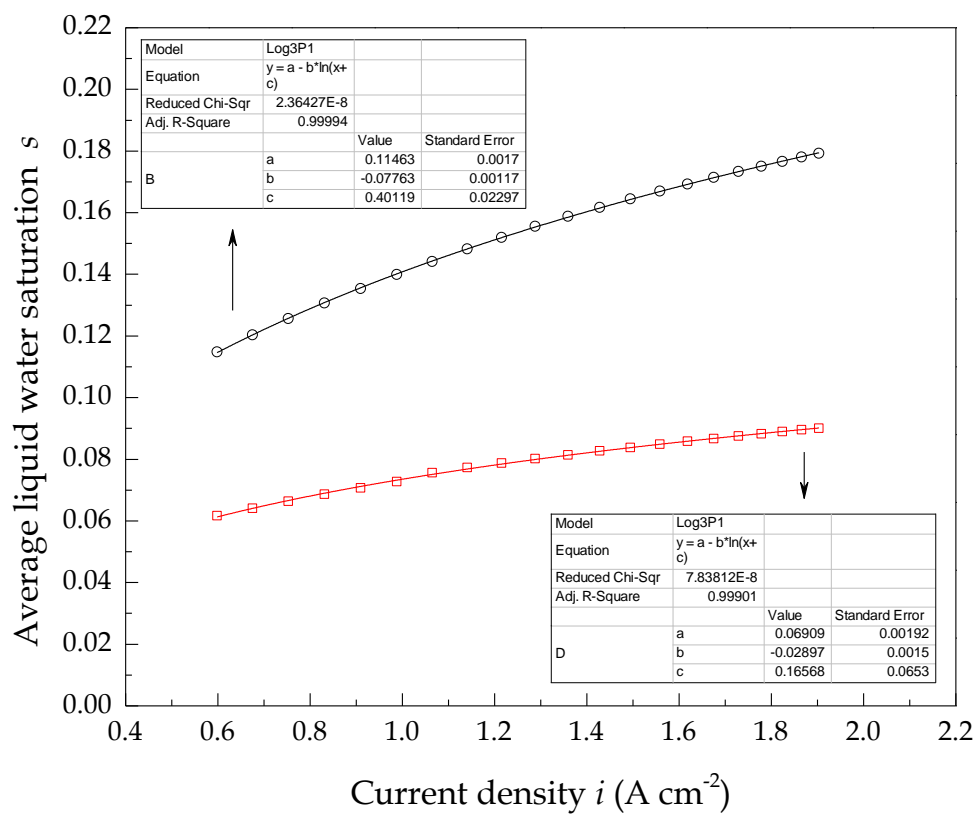| Equation	y = a + b*x	
Weight	No Weighting	
Residual Sum of Squares	5.32715E-10	
Pearson's r	1	
Adj. R-Square	0.99999	
	Value	Standard Error
F Intercept	-1.45542E-4	1.70445E-5
Slope	3.65764	0.0057

Equation	y = a + b*x	
Weight	No Weighting	
Residual Sum of Squares	3.01859E-5	
Pearson's r	0.99961	
Adj. R-Square	0.9992	
	Value	Standard Error
B Intercept	-0.03044	9.07394E-4
Slope	2.32873	0.01247

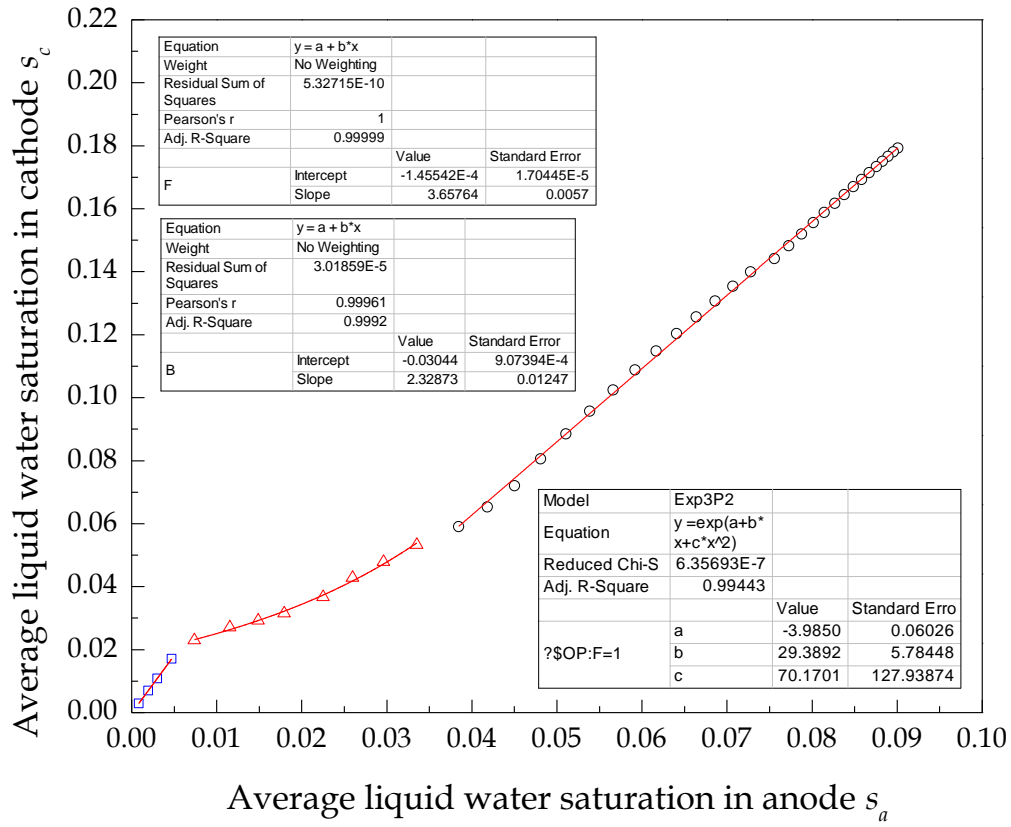| Model	Exp3P2		
Equation	y =exp(a+b* x+c*x^2)		
Reduced Chi-S	6.35693E-7		
Adj. R-Square	0.99443		
		Value	Standard Erro
?$OP:F=1	a	-3.9850	0.06026
	b	29.3892	5.78448
	c	70.1701	127.93874

669

670

671 Fig. 15 Relationship between the average liquid water saturation in the anode and the cathode

672

673

674

675 Table 1 Conservation of water in different phases

676

	Channels	GDLs	CLs
Water vapour S_w^v	$- S_w^{vl}$	$- S_w^{vl}$	$- S_w^{vd} - S_w^{vl}$
Liquid water S_w^l	S_w^{vl}	S_w^{vl}	$S_w^{dl} + S_w^{vl}$
Dissolved water S_w^d	0	0	$S_w^{r,i} + S_w^{vd} - S_w^{dl}$

677 Note: superscript i represents the anode or cathode, the unit for each source term is (mol m^{-3} s^{-1}).

678

679

680

681

682

683   Table 2 Conservation of heat

Membr	CLs	GDLs	Channels
S_T^M	$S_T^{dl} + S_T^{vl} + S_T^{vd} + S_T^{r,i} + S_T^{s,i} + S_T^M$	$S_T^{vl} + S_T^{s,i}$	S_T^{vl}

684   Note: superscript i represents the anode or cathode, the unit for each source term is (W m^{-3}).

685

686

687   Table 3 Source terms

Source terms	Unit	Domain
$S_m = M_{H_2} S_{H_2}^g + M_{O_2} S_{O_2}^g + M_w S_w^v$	kg m^{-3} s^{-1}	GDLs, CLs and channels
$S_{H_2}^g = \dfrac{i_a}{2F}$	mol m^{-3} s^{-1}	ACL
$S_{O_2}^g = \dfrac{i_c}{4F}$	mol m^{-3} s^{-1}	CCL
$S_w^{rc} = \dfrac{i_c}{2F}$	mol m^{-3} s^{-1}	CCL
$S_w^{vd} = k_{ads}(c_w^{eq} - c_w^d) \qquad c_w^d < c_w^{eq}$	mol m^{-3} s^{-1}	ACL and CCL
$S_w^{dl} = k_{des}(c_w^d - c_w^{eq}) \qquad c_w^d \geq c_w^{eq}$	mol m^{-3} s^{-1}	ACL and CCL
$S_T^{sa} = \dfrac{i_a^2}{\sigma_{GDL,a}^{eff}}$	W m^{-3}	Anode GDL
$S_T^{sc} = \dfrac{i_c^2}{\sigma_{GDL,c}^{eff}}$	W m^{-3}	Cathode GDL
$S_T^M = \dfrac{i_M^2}{\sigma_M^{eff}}$	W m^{-3}	Membrane, ACL and CCL
$S_T^{ra} = -|i_a|[\dfrac{T\nabla S_a}{2F}]$	W m^{-3}	ACL
$S_T^{rc} = |i_c|[|\eta_c| - \dfrac{T\nabla S_c}{4F}]$	W m^{-3}	CCL
$S_T^{vd} = M_w S_w^{vd} \nabla h_w^{vd}$	W m^{-3}	ACL and CCL
$S_T^{dl} = M_w S_w^{dl} \nabla h_w^{dl}$	W m^{-3}	ACL and CCL
$S_T^{vl} = M_w S_w^{vl} \nabla h_w^{vl}$	W m^{-3}	CLs, GDLs and channels
$S_w^{vl} = \begin{cases} k_{con} \dfrac{\varepsilon(1-s)x_w^g}{RT}(x_w^g p^g - p_{sat}) & x_w^g p^g \geq p_{sat} \\ k_{eva} \dfrac{\varepsilon s \rho_w^l}{M_w}(p_{sat} - x_w^g p^g) & x_w^g p^g < p_{sat} \end{cases}$	mol m^{-3} s^{-1}	CLs, GDLs and channels

688

689

690

691

Table 4 Expressions of key parameters

Description	Expression	Reference
Volume fraction of Pt/C	$L_{Pt/C} = \dfrac{m_{Pt}}{l_{CL}}(\dfrac{1}{\rho_{Pt}} + \dfrac{1-f}{f}\dfrac{1}{\rho_C})$	[36]
Porosity of catalyst layer	$\varepsilon_{CL} = 1 - L_M - L_{GDL}(1 - \varepsilon_{GDL}) - L_{Pt/C}$	[36]
Agglomerate density of catalyst layer	$N_{agg} = \dfrac{3L_{Pt/C}}{4(1-\varepsilon_{CL})\pi r_{agg}^3}$	[36]
Specific area of agglomerate	$a_{agg} = \dfrac{m_{Pt}A_s}{l_{CL}}\dfrac{(1-\varepsilon_{CL})}{L_{Pt/C}}$	[36]
Reaction surface area per unit platinum mass	$A_s = (227.79f^3 - 158.57f^2 - 201.53f + 159.5)\times 10^3$	[38]
Dry ionomer film thickness surrounding the agglomerate	$\delta_M = r_{agg}(\sqrt[3]{\dfrac{(1-\varepsilon_{CL})(1-\varepsilon_{CL}-L_S) + L_{Pt/C}\varepsilon_{CL}(1-\%M)}{L_{Pt/C}}} - 1)$	[38]
Liquid water film thickness surrounding the agglomerate	$\delta_w = \sqrt[3]{(r_{agg}+\delta_M)^3 + \dfrac{s\varepsilon_{CL}(1-\varepsilon_{CL})r_{agg}^3}{L_{Pt/C}}} - (r_{agg}+\delta_M)$	[38]
Concentration of dissolved water	$c_w^d = \rho_M\lambda/EW(1+k_s\lambda)$	[27]
Water content	$\lambda = 0.043 + 17.81\alpha_w - 39.85\alpha_w^2 + 36.0\alpha_w^3$	[35]
Water activity	$\alpha_w = x_w p/p_{sat} + 2s$	[14]
Vapor saturation pressure	$p_{sat} = 9.531\times10^{-4}(T-237)^4 - 3.123\times10^{-2}(T-237)^3$ $+ 3.451(T-237)^2 + 20.96(T-237) + 611.0$	[35-39]
Effective electronic conductivity of catalyst layer	$\sigma_s^{eff} = (L_{Pt/C})^{1.5}\sigma_s$	[37-39]
Effective ionic conductivity of catalyst layer	$\sigma_M^{eff} = (1-\varepsilon_{CL})\left[1 + \dfrac{(\%M\varepsilon_{CL}-1)}{(1+\delta/r_{agg}+a_0)^3}\right]\sigma_M$	[37-39]
Knudsen diffusivity of species i	$D_{Kn} = \dfrac{d_{avg}}{3}\sqrt{\dfrac{8R_g T}{\pi M_i}}$	[36]

Intrinsic diffusivity of species i	$D_{i-g}^0 = \dfrac{1-x_i}{\sum\limits_{j \neq i}^{n} x_j / D_{i-j}^0}$					[36]
Equivalent diffusivity of species i	$D_{i-P}^0 = \dfrac{D_{i-g}^0 D_{Kn}}{D_{i-g}^0 + D_{Kn}}$					[36]
Diffusivity of oxygen through ionomer film	$D_{O_2-M} = 1.3926 \times 10^{-10} \lambda^{0.708} \exp(\dfrac{T-273}{106.65})$ $-1.6461 \times 10^{-10} \lambda^{0.708} + 5.2 \times 10^{-10}$					[38]

694

695

696 Table 5 Mesh characters

697

698

	Channe	GDLs	CLs	Membr	Total elements
Grid 1	10	10	10	10	17500
Grid 2	30	10	10	10	27500
Grid 3	50	10	10	10	37500
Grid 4	50	30	10	10	47500
Grid 5	50	50	10	10	57500
Grid 6	50	50	30	10	67500
Grid 7	50	50	50	10	77500
Grid 8	50	50	50	50	87500
Grid 9	50	50	50	90	97500

699

700

701   Table 6 Parameters used for model validation and base case condition in the study

702

Symbol	Description (unit)	In house	Wang [41]	Base case
δ_{GDL}	GDL thickness (m)	3.0×10^{-4}	3.0×10^{-4}	3.8×10^{-4}
δ_{CL}	CL thickness (m)	1.5×10^{-5}	1.29×10^{-5}	1.5×10^{-5}
δ_M	Membrane thickness (m)	5.5×10^{-5}	1.08×10^{-4}	1.2×10^{-4}
ε_{GDL}	GDL porosity	0.40	0.40	0.40
m_{Pt}	Platinum loading (mg cm^{-2})	0.10 (anode) 0.40	0.40	0.40
f	Platinum mass ratio	20%	40%	40%
L_M	Volume fraction of ionomer	13.3%	32.5%	40%
T	Operating temperature (°C)	80.0	70.0	70.0
p	Operating pressure (atm)	1.0	1.0	1.0
α_c	Cathode transfer coefficient	0.6	2.0	0.7
r_{agg}	Agglomerate radius (m)	1.0×10^{-6}	1.0×10^{-6}	1.0×10^{-6}

703
704

Table 7 Terms of thermal sources at various current densities with a single PEMFC

Thermal source ($W\ m^{-3}$)	0.2 A cm^{-2}		0.6 A cm^{-2}		1.0 A cm^{-2}	
	Anode	Cathode	Anode	Cathode	Anode	Cathode
S_{vd}^T	4.88×10^6 (11.36%)	2.04×10^6 (1.04%)	5.46×10^6 (4.56%)	3.23×10^5 (0.053%)	5.54×10^6 (2.84%)	7.93×10^3 (0.00078
S_{dl}^T	2.09×10^3 (0.0049%)	1.80×10^6 (0.92%)	4.55×10^3 (0.0038	2.78×10^7 (4.58%)	1.38×10^3 (0.00071	6.23×10^7 (6.11%)
S_{vl}^T	6.85×10^4 (0.16%)	9.89×10^4 (0.051%	2.08×10^5 (0.17%)	3.03×10^5 (0.050%	3.49×10^5 (0.18%)	5.15×10^5 (0.051%
S_{HOR}^T	-3.80×10^7	----	-1.14×10^8	---	-1.89×10^8	---
S_{ORR}^T	---	1.91×10^8 (97.82%	---	5.76×10^8 (94.88%	---	9.50×10^8 (93.15%
S_s^T	3.33×10^3 (0.0078	3.16×10^3 (0.0016	3.02×10^4 (0.025%	2.86×10^4 (0.0047	8.23×10^4 (0.042%	7.81×10^4 (0.0077
$S_{M,i}^T$	9.65×10^3 (0.023%	3.15×10^5 (0.16%)	8.66×10^4 (0.072%	2.65×10^6 (0.44%)	2.34×10^5 (0.12%)	6.91×10^6 (0.68%)
Total	4.30×10^7	1.95×10^8	1.20×10^8	6.07×10^8	1.95×10^8	1.02×10^9

Note: total means the sum of the absolute value of each item; the values in brackets are the percentage of each item corresponded to the total heat of the anode and cathode, respectively.